Applications in Energy and Combustion Science 23 (2025) 100340

Contents lists available at ScienceDirect

Applications in Energy and Combustion Science

journal homepage: www.elsevier.com/locate/jaecs

A computer vision approach for analysis of detonation cellular structures

Daniel Jalontzki [a], Alon Zussman [a,b], Sumedh Pendurkar [c], Guni Sharon [c], Yoram Kozak [a,*]

[a] School of Mechanical Engineering, Tel Aviv University, Tel Aviv, 69978, Israel
[b] School of Electrical Engineering, Tel Aviv University, Tel Aviv, 69978, Israel
[c] Department of Computer Science & Engineering, Texas A&M University, College Station, 77843, TX, USA

ARTICLE INFO

Keywords:
Detonation
Cellular structure
Computer vision
Soot foil analysis
Cell size

ABSTRACT

In the current study, we present a novel computer-vision-based method for automated detection, measurement, and statistical analysis of detonation cellular structure images. The new approach consists of four primary steps: (1) image preprocessing, (2) cell contour detection, (3) parameter optimization, and (4) statistical analysis. First, the cell size measurements from the proposed approach are extensively validated against other measurement methods for numerical soot foils. We demonstrate that the computer vision approach can measure the average cell dimensions with a maximum relative error of 30% for images with a very wide range of cell regularity levels and resolutions. For high-resolution regular and irregular patterned numerical soot foil images, the maximum relative errors decrease to 8% and 17%, respectively. Moreover, cell distribution histogram analysis is carried out for cases with irregular cellular structures. We show that the suggested method can capture the correct cell size distributions with reasonable accuracy in comparison with other measurement methods. Finally, we demonstrate the new computer vision approach capability to automatically analyze high-quality experimentally-derived detonation cellular structure images.

1. Introduction

Gas-phase and liquid spray detonation waves are known for their unstable propagation [1,2]. Although in many cases the detonation wave average speed is constant and remarkably agrees with the classical Chapman–Jouguet (CJ) theory [3], the wave front local speed is governed by highly unsteady triple-shock interactions [4]. As such, the incident shock interacts with transverse waves leading to a localized explosion that forms a Mach stem. The maximum pressure produced by these reactive shock interactions is usually found at the triple point which connects the three shock waves. The triple point trajectories commonly produce complex cellular structures that resemble fish scales [5]. It is well-established that the average detonation cell width, typically denoted as λ, is associated with detonation wave's ability to propagate through thin tubes or channels, as well as the critical tube diameter and detonation direct initiation energy, see for instance [6]. Moreover, the detonation cell size distribution, which can range from very regular to highly-irregular, can also affect the above-mentioned detonation properties, see for instance [7].

Experimental measurement of cellular detonation structures is usually carried out via soot-covered foils that are placed at the inner side of the confinement (tube or channel) [8]. The high localized pressure variations in the vicinity of the triple points leave visible markings on the soot foil that reveal the detonation wave cellular structure, see for instance [7]. Another possible technique for cell size measurements is open-shutter photography, where luminescence induced at the triple points is directly photographed [9]. Although this technique is limited to certain mixtures, such as acetylene-oxygen, it can produce high-quality images of the detonation cellular structures, see for instance [10,11]. The practical importance of the detonation cell width has driven extensive experimental measurements under a variety of conditions, see for instance [2,12–20]. In addition, multi-dimensional numerical simulations can also produce cellular structures similar to those observed in experiments, thus providing further insights on the detonation wave dynamics. Due to the high computational cost, most numerical simulations are two-dimensional with either single-step [21–29] or multi-step [30–34] chemical kinetics. However, the detonation cellular structure has also been explored by highly computationally expensive three-dimensional numerical simulations, see for instance [35–38].

For both experiments and numerical simulations, the resulting cellular structure is measured from an image. Typically, cell dimensions are measured manually, either by finding the distances between triple point tracks or by discretely measuring each cell dimensions, see for instance [39]. In either case, the quality of the observed cellular structures can significantly differ between images depending on the chosen

* Corresponding author.
E-mail address: kozaky@tauex.tau.ac.il (Y. Kozak).

https://doi.org/10.1016/j.jaecs.2025.100340
Received 24 December 2024; Received in revised form 26 May 2025; Accepted 26 May 2025
Available online 10 June 2025

experimental technique, level of cell regularity, and image rendering technique for numerical soot foils. As a result, it is well-established that manual measurements are prone to subjective measurement errors of up to 100%, see for instance [6]. In addition, manual measurements of detonation cells can be time-consuming and tedious. Also, it should be noted that currently there are no standardized approaches for deriving experimental or numerical images of cellular structures. Thus, attaining reliable and accurate manual measurements of detonation cellular structures, whether experimentally or numerically, still remains highly challenging.

To overcome the above-mentioned limitations of manual measurements, different automated techniques were developed for quicker and more objective detonation cell size measurements. The first automated framework for cell size measurements was developed by Shepherd and Tieszen [40]. A digital image processing technique was utilized for analyzing experimental soot foils. The power spectral density of the cellular structure was obtained using a two-dimensional spectral analysis. Then, the most dominant cell width was found from a one-dimensional projection of the spectral density. The suggested technique was later utilized by Shepherd et al. [41] for analyzing experimental soot foils of gas-phase detonations in a variety of mixtures. Each soot foil was photographed, digitized, and enhanced. Then, using a Fast Fourier Transform (FFT), the cell size was derived according to the resulting spectra. Lee et al. [42] analyzed experimental soot foils using a one-dimensional autocorrelation function. For this purpose, the cellular structure observed in the soot foils was hand-drawn and digitized. Then, histogram and statistical analysis of the cell sizes was carried out for detonations in various mixtures. This technique was later improved by Lee et al. [43] using a two-dimensional autocorrelation function for quantifying the cell size and level of regularity. Sharpe and Radulescu [22] developed two different methods for analyzing numerical soot foils. Both methods relied on signed vorticity records for identifying the triple point trajectories. The spacings between triple point tracks were calculated either directly or by an autocorrelation function. The two methods were used to statistically analyze irregular cellular structures obtained via gas-phase detonation numerical simulations with single-step chemical kinetics. Very recently, Sharma et al. [44] developed a machine-learning-based approach to determine detonation cell size in either numerical or experimental soot foil images. The method involves an image preprocessing step followed by a modified image segmentation technique based on cellular biology segmentation models. It has been demonstrated that the new machine learning approach can detect and measure cell sizes from a wide range of known detonation cellular structure images. It should be noted that although different automatic approaches were suggested in the past, there is still no standardized automatic method for detonation cell measurements. As a result, in many cases, manual measurements, which involve subjective errors, are still used.

Computer vision is a sub-field of Artificial Intelligence (AI) that deals with analysis of digital images and data extraction, see for instance [45,46]. Today, computer-vision-based techniques and algorithms are commonly used to tackle a variety of practical fluid mechanics problems. Examples include analysis of air flows [47], measurements of free surface wave displacements [48], extraction of liquid droplet shapes [49], analysis of high-temperature plasma flows [50], characterization of bubble dynamics [51], and tracking of gravity current features [52]. For analysis of detonation cellular structure images, the main uses of computer vision techniques focused on image denoising and filtering, see for instance [53], automatic feature extraction via spectral methods [22,40–43], and assistance in manual cell size measurements, see for instance [23]. Also, Sharma et al. [44] carried out soot foil segmentation using a machine-learning-based computer vision technique. However, many of existing computer vision algorithms and techniques had still never been used for measuring and analyzing images of detonation cellular structures. Our goal is to propose a new automatic detonation cell measurement method, which is based on algorithmic computer vision techniques. As such, the current study will pave the way for a standardized measurement approach.

To address the above-mentioned research gaps, we develop a novel computer-vision-based framework that can automatically detect, measure, and analyze images of detonation cellular structures obtained either numerically or experimentally. As the new approach is completely automatic, subjective measurement errors of cell dimensions can be avoided. In addition, the laborious and time consuming task of manually measuring and statistically analyzing detonation cell dimensions can be replaced using a standard laptop computer. In the next sections, we describe our newly suggested approach in detail and extensively validate its results against a variety of cases from the literature.

2. Proposed method

In this section, we present the general framework for our newly proposed automated detonation cell size detection algorithm. This approach, based on widely used techniques within the computer vision domain, comprises four primary steps: image preprocessing, cell contour detection, parameter optimization, and statistical analysis. The source code for the suggested computer vision detonation cell detection approach will be publicly available in an online repository.

2.1. Image preprocessing

The initial step involves image preprocessing, which aims to enhance the accuracy of cell size measurements. This process, implemented using methods from the OpenCV library, comprises two primary steps: contrast enhancement and image denoising [54]. Note that the computer vision techniques chosen for the image preprocessing step were found to be optimal by empirical trial-and-error across many possible variations. The proposed set of image preprocessing methods and parameters is applied to all the cellular detonation structure images analyzed in the current work.

2.1.1. Contrast enhancement

To improve the visibility of cellular structures formed by detonation waves, we first apply a local contrast enhancement technique to the detonation cellular structure image. The purpose of this procedure is to make subtle features, such as cell boundaries and details within the cell structures, more distinguishable.

An image processing technique commonly used for improving local contrast and enhancing the definitions of edges is the *Adaptive Histogram Equalization* (AHE) [55]. This technique uses histogram representation of the image and divides it into smaller blocks or "tiles". Then, for each block, histogram equalization is carried out. Thus, pixel intensities are redistributed within each block to spread out the most frequent intensity values and improve contrast in that specific region.

However, AHE may lead to over-amplification of noise [55], especially in images with varying local contrast, which is often seen in soot foil images. To address this issue, we convert the image from RGB color space to gray-scale and use the *Contrast Limited Adaptive Histogram Equalization* (CLAHE) technique, which is a variation of AHE. The key advantage of CLAHE is that it prevents over-amplification of noise by limiting the contrast in each region [56]. The CLAHE technique is controlled by two parameters: clipping limit and tile grid size. Increasing the clipping limit may result in more prominent and clearly-visible cellular edges; however, it may amplify noise and generate artifacts. Similarly, decreasing the tile grid size may adapt better to rapidly varying edge intensities (for example, in highly dense soot foil images); however, it may increase noise and the appearance of unwanted artifacts. As such, the clipping limit is set to 2.0, with a tile grid size of 8.0 pixels. These values were found to be most effective in improving the visibility of faint cellular structures while minimizing noise amplification. Fig. 1 demonstrates the effect of the

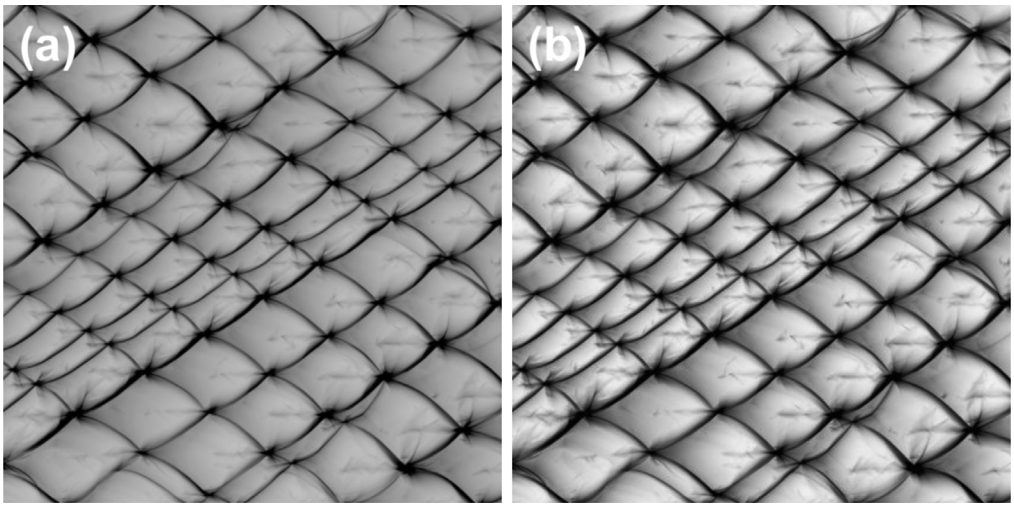

Fig. 1. A numerical soot foil image from Zadok et al. [21] (a) before and (b) after applying the CLAHE technique.

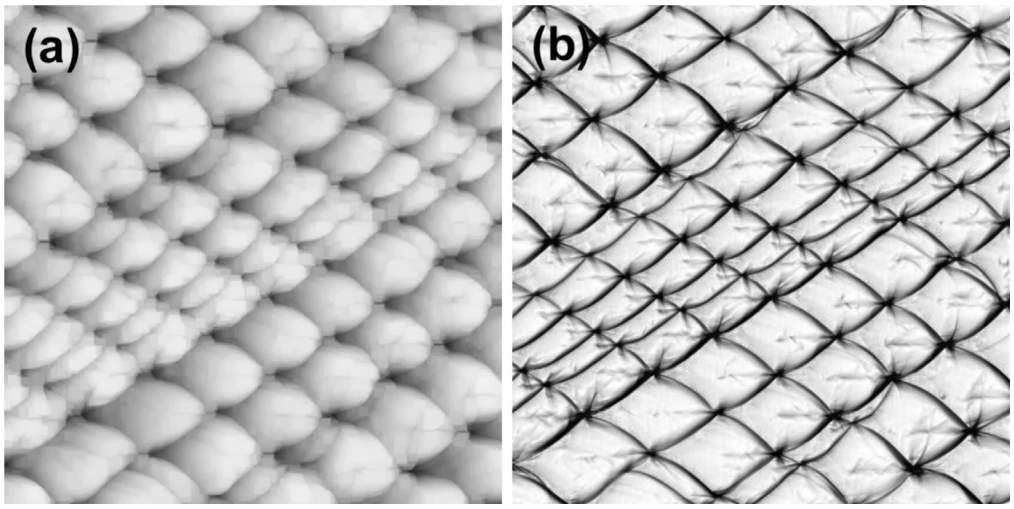

Fig. 2. Preprocessed numerical soot foil image after (a) dilation operation and (b) division operation.

CLAHE technique on a typical numerical soot foil from the work by Zadok et al. [21].

Subsequently, a gray-scale dilation operation, which expands bright regions within the image, is performed on the contrast-enhanced image using a flat structuring element with dimensions of 8 × 8 pixels [57]:

$$(f \oplus b)(x,y) = \max_{(s,t)\in b}\{f(x-s,y-t)\}, \tag{1}$$

where $f(x,y)$ is the contrast-enhanced image intensity at point (x,y), which is dilated by the structuring element b at coordinates (s,t). The resulting image after the dilation operation is depicted in Fig. 2a.

Then, we employ a pixel-wise division operation between the contrast-enhanced image and the dilated image to normalize illumination variations in the image:

$$R(x,y) = \frac{I_c(x,y)}{I_d(x,y)} \times 255, \tag{2}$$

where $I_c(x,y)$ and $I_d(x,y)$ are the contrast-enhanced image and the dilated version of $I_c(x,y)$, respectively. The resulting image is shown in Fig. 2b.

Finally, the resulting image undergoes thresholding using *Otsu's method* [58]. This step converts the image into a binary format (0 for black and 1 for white), effectively distinguishing foreground from background based on intensity.

2.1.2. Image denoising

For image denoising, a non-local means image denoising algorithm is implemented, see [59]. This advanced denoising technique mitigates noise while preserving critical edges and details within the image. For this purpose, we use the parameters recommended by the OpenCV documentation, see [54]. The final manipulated image is shown in Fig. 3.

2.2. Contour detection

For identifying the cellular structures in the preprocessed image, we use the Suzuki and Abe contour detection algorithm for binary images, see [60]. By scanning the image row by row, pixel by pixel, the algorithm identifies a set of adjacent pixels that share the same intensity or color, which are referred to as connected components. The algorithm finds the first black pixel (edge) and follows the chain of neighboring black pixels until it returns to the starting point, forming a closed contour. The Suzuki and Abe algorithm can also be used with specified minimum and maximum contour area thresholds to exclude structures that fall outside this range. The computational cost of the algorithm is relatively low, making it suitable for real-time applications and large-scale image processing tasks. In addition, the algorithm can handle images with noise, gaps, and partial occlusions [60].

Fig. 3. Final output image after the preprocessing stage.

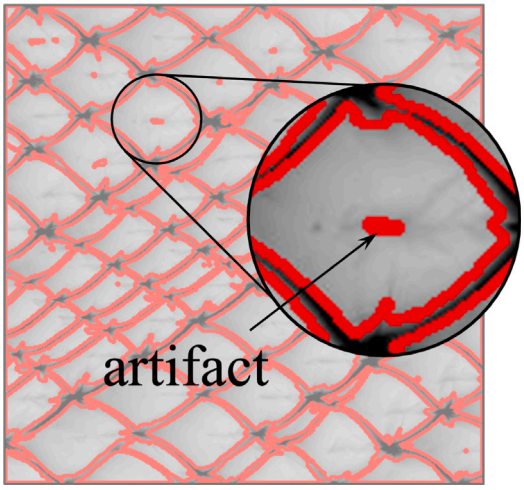

Fig. 4. Contour detection before applying area filtering, showing the identification of amorphous artifacts (an example is shown in circle).

The resulting image, after applying the Suzuki and Abe algorithm, is presented in Fig. 4. While the fundamental cell structure is well defined and identified, some artifacts are observed, likely resulting from high-pressure points within the cell structure. Yet, the detection of such abstract structures can be avoided by setting appropriate minimum and maximum area threshold values for contour detection, as mentioned above. As a result, structures that fall outside this range are filtered out. In the next section, we present an optimization algorithm that automatically selects the best minimum and maximum area threshold values based on the proximity of adjacent cell corners.

2.3. Parameter optimization

As mentioned in the section above, a key step in fully automating the cell size measurement procedure is to find the optimal minimum and maximum area threshold values in the contour detection process. For this purpose, we define a junction as the situation where the bottom, left, top, and right corners of the top, right, bottom, and left cells, respectively, are found within a specified radius, r, which is calculated by using Eq. (3) (see also Fig. 5):

$$r = \sqrt{A/\pi}, \tag{3}$$

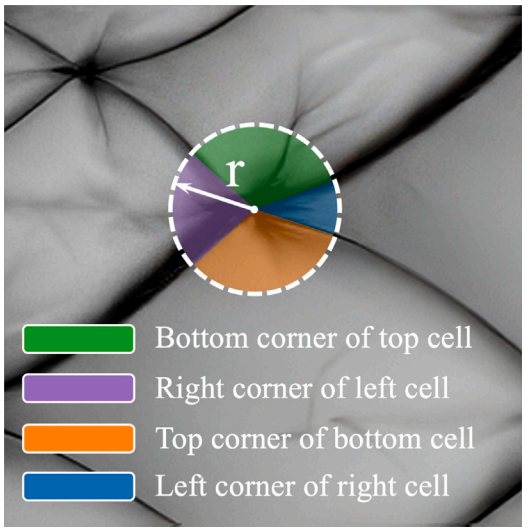

Fig. 5. Illustration of a junction overlaid on a numerical soot foil magnified view.

where A is the minimum or maximum area value. All the steps for searching and finding the junctions are described in detail in Algorithm 1. In particular, the algorithm receives the lists of all the top, bottom, left and right corners of the detected cells, following the contour detection process. Additionally, it receives the value of the minimum or maximum cell area, A, to determine the criterion for the junction identification, as introduced in Eq. (3). Then, it outputs a list of all the junctions found in the image.

Algorithm 1: Junction search.

```
Input: top.list, bottom.list, left.list, right.list, A (min.area or
       max.area)
r ← (A/π)^{1/2};
foreach top ∈ top.list do
    foreach bottom ∈ bottom.list do
        if distance(top, bottom) ≤ r then
            foreach left ∈ left.list do
                if distance(top, left) ≤ r then
                    foreach right ∈ right.list do
                        if distance(top, right) ≤ r then
                            Add top, bottom, left, right to jun.list;
                        end
                    end
                end
            end
        end
    end
end
return jun.list, r;
```

The optimization procedure utilizes a modified brute-force search over a range of minimum and maximum area values, $A_{\min}$ and $A_{\max}$, respectively, see also Algorithm 2. For each pair of values, following the contour detection procedure, the algorithm computes the number of junctions. The optimal area values are those who yield the maximum number of junctions. To make the search more efficient, the initial value of $A_{\min}$ is set to be 0, and the initial value of $A_{\max}$ is set to a high number, e.g., total image area. Initially, the algorithm performs a "forward search", in which the value of $A_{\max}$ is fixed and the value of $A_{\min}$ is increased gradually, by increments of 10 pixels. The number of junctions is calculated in each step. As initially the value of A in

Eq. (3) is $A_{min} = 0$, the initial number of junctions is zero. As the search progresses, the value of r also increases. The coupling of both radius and area values of the junctions ensures automatic filtration of structures that are smaller than the radius of each junction, and which are assumed to be artifacts, see Fig. 4. The steps for the "backward search" are identical to those described in Algorithm 2, with the exception that the "for" loop runs from A_{max} down to $A_{min,opt}$ for each value of A. The returned value is then $A_{max,opt}$ which is calculated in the same manner as described in Algorithm 2. Note that the suggested brute-force search approach for the optimization procedure can be replaced by sophisticated and more efficient search techniques, such as a genetic algorithm. However, for all the cases explored in the current study, this improvement is not essential due to the relatively modest computational overhead associated with the current algorithm. Ultimately, the goal of the optimization procedure, by carefully selecting the optimal values of A_{min} and A_{max}, is to effectively eliminate and filter any artifacts that may be detected during the contour detection process.

Algorithm 2: Optimization loop for minimum area.

```
A_max ← height × width;
foreach A_min ∈ {0, ..., A_max} do
    Detect.contours (A_min, A_max) → cell.area, top.list,
      bottom.list, left.list, right.list;
    area.percent ← (cell.area)/A_max;
    if area.percent == 0 then
        break;
    end
    jun.num ← find junctions using algorithm 1;
end
A_min,opt = arg max_{A_min} {jun.num};
return A_min,opt;
```

The resulting image after the optimization procedure is shown in Fig. 6. Note that the current optimization procedure relies on the assumption that each detonation cell has four corners. However, this assumption might not be correct for certain cellular structures. For example, numerical soot foils derived from 3-D simulations with a strong influence of the confinement shape, see for instance, [37], or experimental front views of cellular structures that more resemble polygons, see for instance [61]. Although it is possible to extend the suggested approach to these less common cases, it is beyond the scope of the current work.

2.4. Statistical analysis

To perform statistical analysis of cell sizes, the dimensions of each cell are automatically measured. For this purpose, the top, bottom, right, and left corners of each cell are determined by finding the extremum x and y coordinates for each contour. Then, each cell length and width are calculated as the Euclidean distance (in pixels) between the right and left corners, and top and bottom corners, respectively, see Fig. 7. By specifying the image height or width (provided as an argument to the algorithm) this distance can be converted into length units. The results are automatically presented in a histogram that illustrates the distribution of the cell sizes, alongside the probability density function (PDF) and the cumulative distribution function (CDF). The mean values for both cell length and width are also calculated. In general, statistical results can be computed for a single image or aggregated across multiple images.

3. Results and discussion

In this section, we present an extensive validation and demonstration of the suggested computer-vision-based approach capabilities in detecting and measuring detonation cellular structures from images. In particular, regular and irregular numerical soot foils from the literature are analyzed in detail. Then, all the cell size measurement results are compared against results obtained from prior measurement methods.

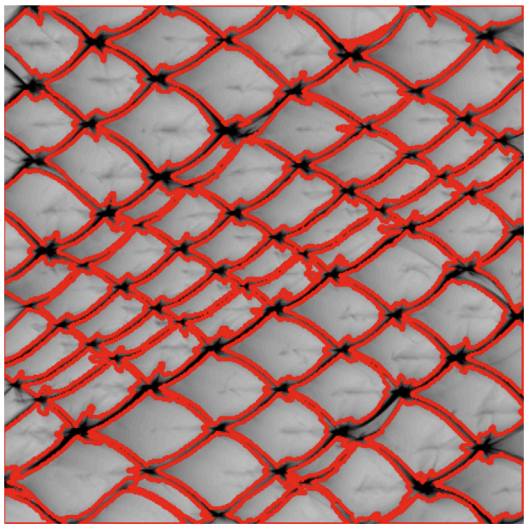

Fig. 6. Final contour detection (red lines) of a numerical soot foil image by Zadok et al. [21]. The minimum and maximum area values for optimal contour detection are selected automatically. (For interpretation of the references to color in this figure legend, the reader is referred to the web version of this article.)

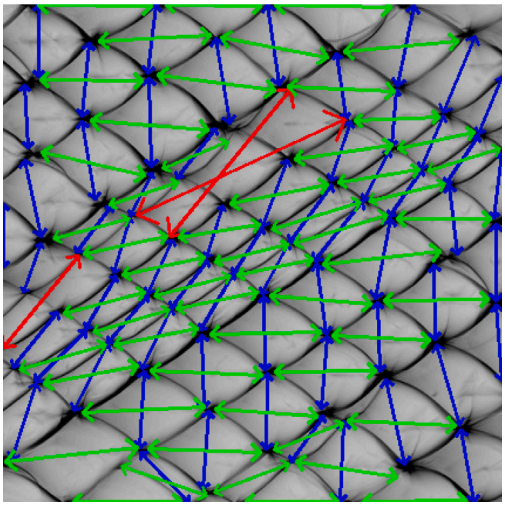

Fig. 7. Automated cell length and cell width measurements used for statistical analysis of a numerical soot foil image by Zadok et al. [21]. Misaligned measurements, caused mainly by merged cells with insufficiently distinguishable borders, are indicated by the red arrows (4.22% out of total measured cells). (For interpretation of the references to color in this figure legend, the reader is referred to the web version of this article.)

3.1. Image resolution and preprocessing sensitivity analysis

As mentioned in Section 2, adequate image preprocessing is key for successful identification of the cellular structure of soot foil images. This step is highly dependent on the image quality, and specifically the amount of noise introduced. In addition to the noise reduction techniques introduced in Section 2.1.2, correctly adjusting the image resolution may also improve the image preprocessing results. Practically, higher image resolution may amplify noise, especially in images with relatively high noise levels. In general, a measure of ~40 pixels/cell size was found empirically to be optimal for balancing image

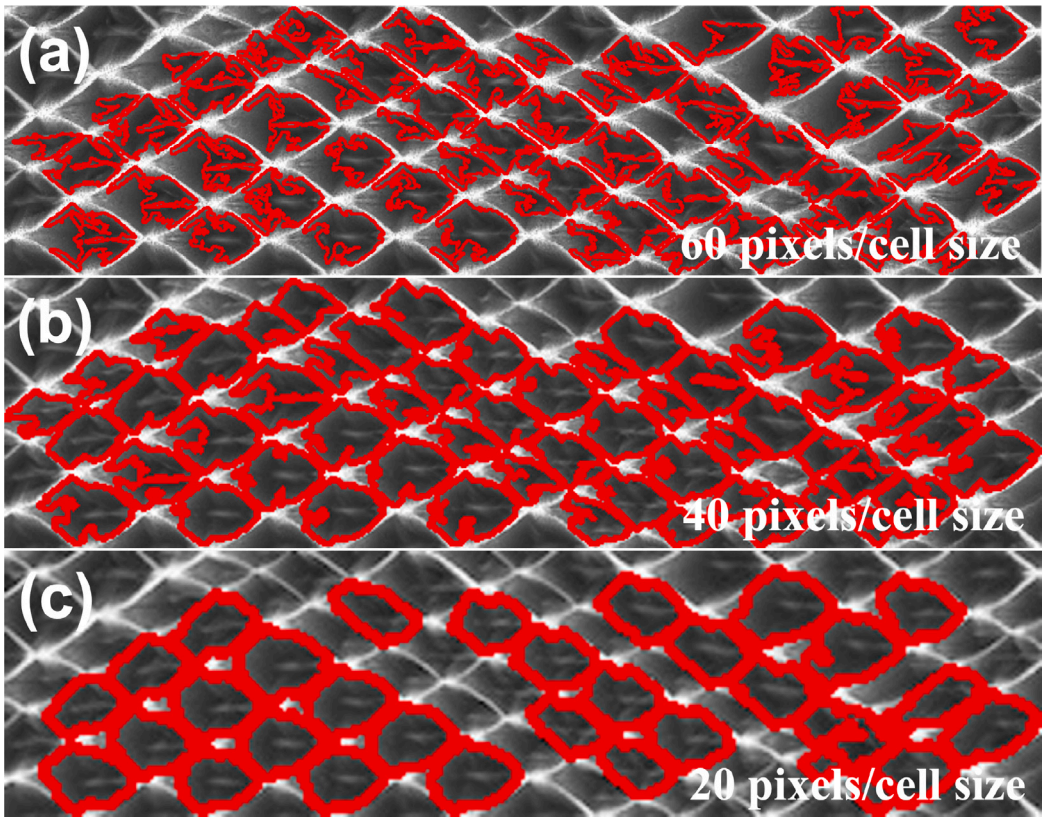

Fig. 8. The effect of image resolution on cell contour detection for a typical soot foil by [37]: (a) High-resolution (~60 pixels/cell size), (b) Medium-resolution (~40 pixels/cell size, and (c) Low-resolution (~20 pixels/cell size). Image resolution of ~40 pixels/cell size was empirically found to be optimal for all cases discussed in this work.

noise reduction and successful cell identification for the majority of the examined soot foils. Fig. 8 depicts how different image resolutions affect the cell identification process in the numerical soot foil image from [37]. In this image, the high-pressure triple points exhibit relatively high noise levels. Using the original image resolution (~60 pixels/cell size) resulted in cell contours having a higher number of obscured shapes. Lowering the image resolution to ~40 pixels/cell size allowed for better cell contour identification as noise levels decreased. However, further lowering the image resolution to ~20 pixels/cell size resulted in a higher number of unidentified cells. This is also reflected in the measured average cell widths, which are 4.58 cm, 5.98 cm, and 7.73 cm for the high-, medium-, and low-resolution soot foil images, respectively. For comparison, the manually measured average cell width is 5.66 cm, corresponding to relative errors of 19%, 5.7%, and 37% for the high-, medium-, and low-resolution images, respectively. In this case, the high-resolution image resulted in smaller measured cells due to obscured or fragmented cell shapes, whereas the low-resolution image failed to identify smaller cells altogether, leading to an overestimation of the average size. Ultimately, the medium-resolution image produced the most accurate measurement, with the lowest relative error. To conclude, for images with a resolution higher than 40 pixels/cell size, lowering the image resolution to the optimal value improves the algorithm's performance. On the other hand, for images with a resolution lower than 40 pixels/cell size, the algorithm's performance degrades. Thus, to achieve optimal performance, the initial image resolution should be equal to or higher than 40 pixels/cell size.

We also demonstrate how the different image preprocessing steps, as introduced in Section 2.1, affect the cell identification results shown in Fig. 7. For example, Fig. 9 shows the computer vision approach results once the CLAHE step is omitted, leading to a greater number of undetected or merged cells. Fig. 10 presents the same test case without the image denoising step. In a similar manner, the number of merged cells increases. This comparison highlights the importance of proper image preprocessing on the algorithm's performance.

3.2. Computational performance analysis

In this section, we analyze the computer vision approach algorithm's computational performance. Thus, several runtime complexity tests are conducted on four different numerical soot foils from Sharpe and Radulescu (Cases A-D) [22]. Each of the soot foils is divided into four subsections of dimensionless size of 96×750. For each case, the algorithm is first executed on the initial subsection, followed by a second execution using the aggregation of the first and second subsections, and so on, until the final execution on the full-scale image. All tests are carried out using a standard laptop computer and a single core. Fig. 11 demonstrates how the runtime of the optimization procedure linearly increases with image size and number of cells.

3.3. Numerical soot foils with a regular cellular structure

In this section, we analyze cell dimensions measurements obtained via the computer vision approach for numerical soot foils with a regular cellular structure. We examine three different numerical soot foils from the work of Zadok et al. [21], which used single-step chemical kinetics and a calorically perfect gas equation of state. As such, for all the cases, the ratio of specific heat capacities, γ, and normalized heat release, $\hat{q}$, are equal to 1.5 and 26.33, respectively. However, the effective activation energy, ε, varies between the different cases with values of 3, 4, and 5. For each case, the numerical soot foil dimensions are 32×32 cm. Fig. 12 presents the three numerical soot foils from Zadok et al. [21], where the computer vision approach cellular structure detection results are overlaid in red. For the cases for which $\varepsilon = 4$ and 5, the cellular structure is perfectly regular, see also Figs. 12(b) and 12(c). For all

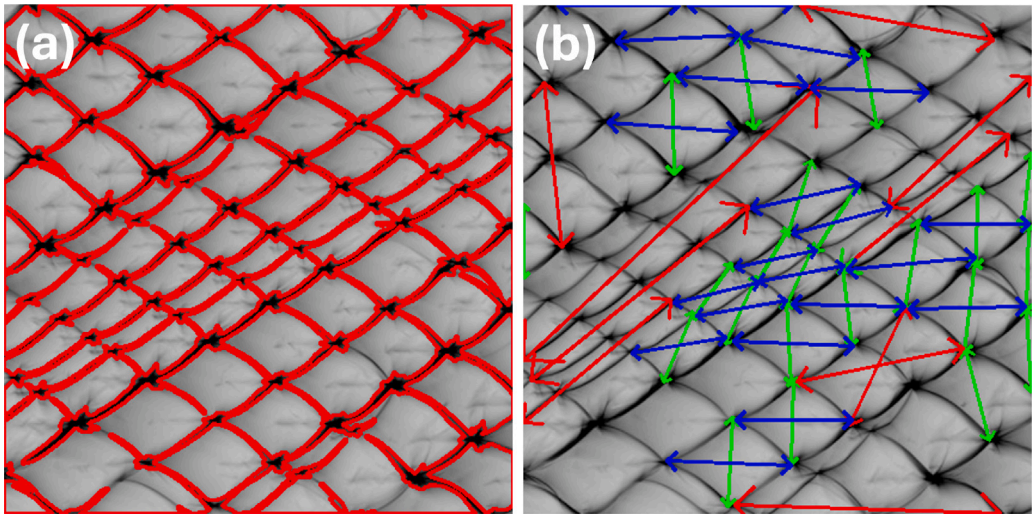

Fig. 9. (a) Automated cell contour detection and (b) Cell size measurements of the soot foil in Fig. 7 without employing CLAHE. Misaligned measurements, caused mainly by merged cells with insufficiently distinguishable borders, are indicated by the red arrows (25.7% out of total measured cells). (For interpretation of the references to color in this figure legend, the reader is referred to the web version of this article.)

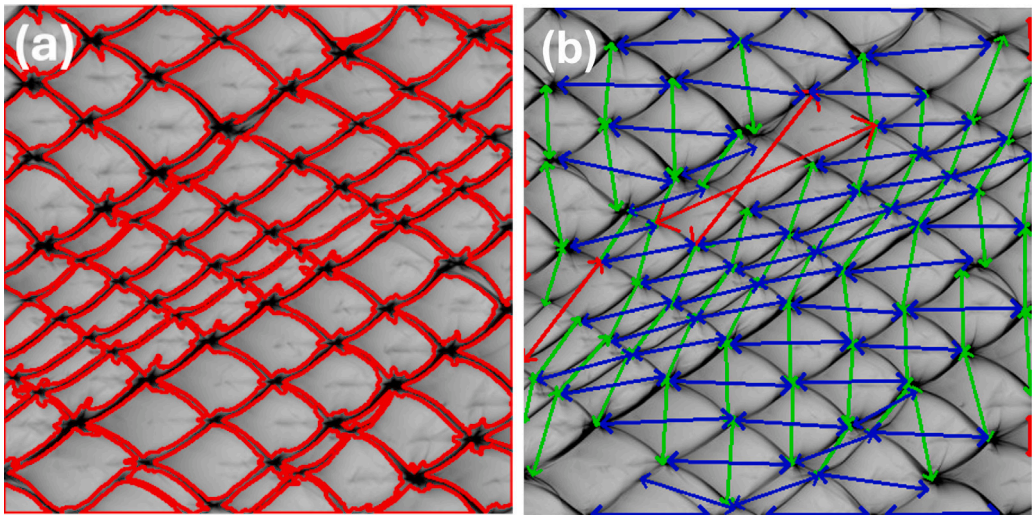

Fig. 10. (a) Automated cell contour detection and (b) Cell size measurements of the soot foil in Fig. 7 without employing image denoising. Misaligned measurements, caused mainly by merged cells with insufficiently distinguishable borders, are indicated by the red arrows (9.84% out of total measured cells). (For interpretation of the references to color in this figure legend, the reader is referred to the web version of this article.)

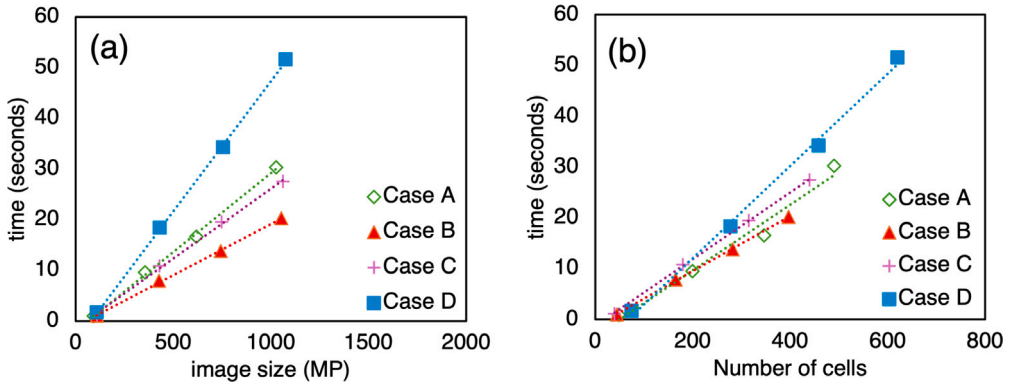

Fig. 11. Algorithm runtime as a function of: (a) Image size and (b) Number of cells. In Cases A-D from [22], each soot foil image is divided into four subsections. The algorithm is first executed on the initial subsection, followed by successive executions on incrementally aggregated subsections, up to the full-scale image.

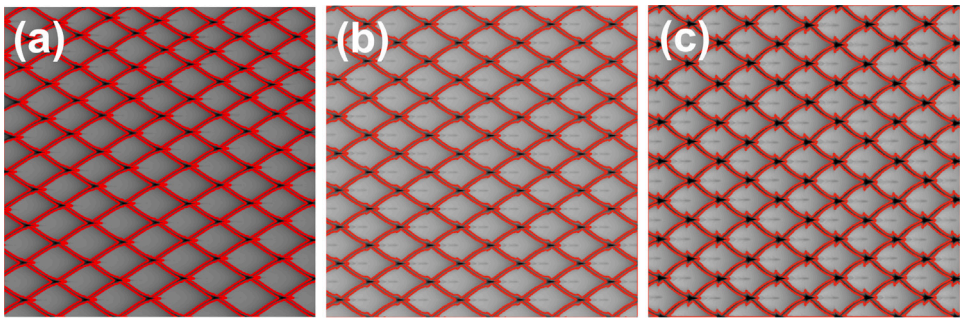

(a) $\varepsilon = 3$ (b) $\varepsilon = 4$ (c) $\varepsilon = 5$

Fig. 12. Numerical soot foils with regular cellular patterns: $\gamma = 1.5$, $\hat{q} = 26.33$, see also Zadok et al. [21]. Computer vision approach cellular structure detection results are overlaid in red. (For interpretation of the references to color in this figure legend, the reader is referred to the web version of this article.)

Table 1
Regular cellular structure numerical soot foil analysis, see also Fig. 12. Comparison between the average cell length, L, and width, λ, measurements obtained manually and by the computer vision approach. The standard deviation for each case is denoted as σ.

Cell dimension	$\varepsilon = 3$		$\varepsilon = 4$		$\varepsilon = 5$	
	L	λ	L	λ	L	λ
Number of cells	80		72		67	
Manual measurement, cm	5.98 ($2\sigma/\lambda = 0.16$)	3.55 ($2\sigma/\lambda = 0.18$)	6.07 ($2\sigma/\lambda = 0.037$)	3.73 ($2\sigma/\lambda = 0.051$)	5.81 ($2\sigma/\lambda = 0.059$)	3.95 ($2\sigma/\lambda = 0.061$)
Computer vision approach, cm	5.75 ($2\sigma/\lambda = 0.18$)	3.64 ($2\sigma/\lambda = 0.20$)	5.85 ($2\sigma/\lambda = 0.019$)	3.77 ($2\sigma/\lambda = 0.071$)	5.88 ($2\sigma/\lambda = 0.037$)	4.26 ($2\sigma/\lambda = 0.034$)
Relative error, %	3.9	2.5	3.6	1.1	1.2	7.9

cases, we compare the computer-vision-based measurements against individual manual measurements for each cell width and length.

Table 1 presents a comparison between the average cell width, λ, and length, L, values obtained by the computer vision approach and manual measurements. For all cases, the computer vision approach is able to correctly capture the average cell dimensions with a relative error of less than 8%.

For the case of $\varepsilon = 3$ from Zadok et al. [21], which does not exhibit a perfectly regular cellular pattern, we carry out a more detailed statistical analysis. Fig. 13(a) shows the manual measurement procedure we carried out for each cell by using "ImageJ", a widely recognized image processing tool in the scientific community that allows manual measurements of the Euclidean distance between two points in a selected image [62]. Fig. 13(b) shows the measurements by the computer vision approach for the same numerical soot foil. The measured cell widths and lengths are indicated in violet and green, respectively. A detailed comparison between the cell width and length distributions obtained manually and by the computer vision approach is shown by histograms in Fig. 14.

3.4. Numerical soot foils with an irregular cellular structure

In this section, we demonstrate the computer vision approach cell detection capabilities for irregular numerical soot foils with different levels of cell regularity that were generated using our own numerical simulations. Furthermore, we compare the results from the computer vision approach against benchmark results from the literature for irregular structured numerical soot foils.

First, we employ the computer vision approach on numerical soot foils generated by 2-D numerical solutions of the reactive compressible Euler equations with single-step chemical kinetics and calorically perfect gas equation of state following [22]. For all the cases, the values of the specific heat capacity ratio, γ, and the normalized heat release, $\hat{q}$, are 1.4 and 25, respectively. Three different values of the effective activation energy, ϵ, are explored: 2.5, 3.75, and 5. As such, the level of cell regularity alters for different values of ϵ. The results for the cell contour detection and the measurements for each case are presented in Fig. 15. The total number of measured cells is 834, 644, and 807 for Fig. 15a, b, and c, respectively. The results suggest that the computer vision approach can accurately measure the cell size for regular as well as irregular numerical soot foils.

Moreover, we compare the computer vision approach measurements, which are illustrated in Figs. 16–19, against the results by the automated signed vorticity records approach suggested by Sharpe and Radulescu [22]. Table 2 presents the measured average normalized cell width for cases with different normalized activation energies E: Case A ($E = 20$), Case B ($E = 25$), Case C ($E = 27$), and Case D ($E = 15$). Note that a higher normalized activation energy increases the cellular structure's irregularity, see for instance [63]. Our analysis shows that all measurements from these cases suggest less than 17% relative error for the average normalized cell width between the computer vision approach and the results reported by Sharpe and Radulescu [22].

A key feature of the computer vision approach is its ability to provide discrete values for the cell dimensions. We further analyze differences between the computer vision approach and the method suggested by Sharpe and Radulescu [22], which is based on measuring distances between triple point tracks. Fig. 20 compares the Probability Density Functions (PDF) for the cell width distributions for Cases A-D as obtained from Sharpe and Radulescu [22] with the histograms provided by the computer vision algorithm. For normalized cell widths, also referred to as "spacing", larger than 10, the general trends in the cell size distribution are very similar for both methods. Also, for Case D, which exhibits the most regular cellular structure, the agreement between the two methods is very good. However, the probabilities of the cell size distributions obtained by the two methods are different for Cases A-C. The reason for this is twofold. First, it is evident that the computer vision approach cannot identify some of the smallest cellular structures, especially for very irregular cases, see Figs. 16–18. Second, these differences are associated with the fact that the PDFs for Cases A-C suggest the existence of cells with spacings approaching zero, even though it is evident that such small cells do not appear in these numerical soot foils. Thus, some of the discrepancies are due to the fact that the method by Sharpe and Radulescu [22] analyzes the spacings between neighboring triple point tracks rather than the discrete width

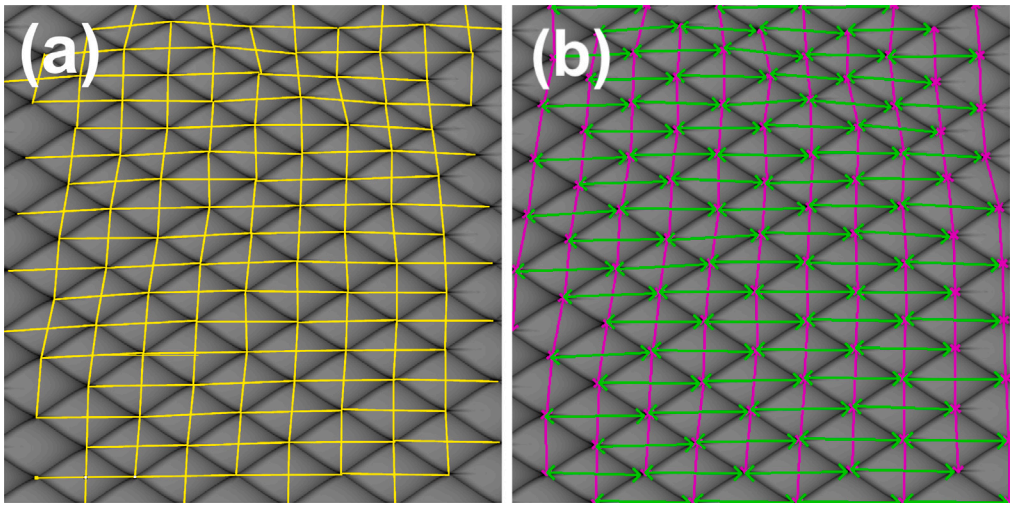

Fig. 13. Cell dimensions measurements for the case of $\varepsilon = 3$ from Zadok et al. [21]: (a) Manual measurements, and (b) Computer vision approach measurements. (For interpretation of the references to color in this figure legend, the reader is referred to the web version of this article.)

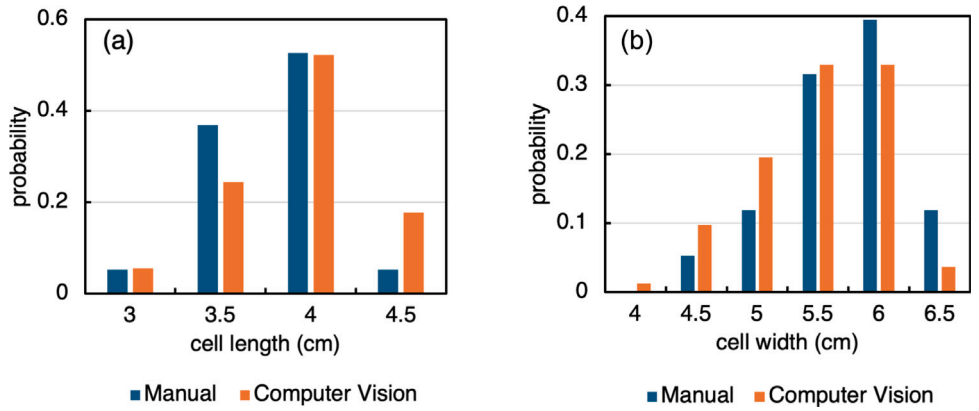

Fig. 14. Comparison by histograms between manually and computer vision approach measured cell dimensions distributions for the case of $\varepsilon = 3$ from Zadok et al. [21]: (a) Cell length and (b) Cell width.

Table 2
Average cell width: Comparison between the measurements according to the computer vision approach and the results by Sharpe and Radulescu [22]. The measured standard deviation is denoted as σ.

	Case A $E = 20$	Case B $E = 25$	Case C $E = 27$	Case D $E = 15$
Sharpe and Radulescu [22]	21.0 (σ = 7.2)	22.0 (σ = 9.4)	22.0 (σ = 9.7)	19.0 (σ = 3.2)
Computer vision approach	24.5 (σ = 7.8)	24.1 (σ = 8.09)	22.1 (σ = 7.59)	16.9 (σ = 3.34)
Total number of cells	**490**	**397**	**440**	**621**
Cell regularity ($2\sigma/\lambda$)	**0.64**	**0.67**	**0.69**	**0.39**
Relative error, %	17	10	0.5	11

associated with each cell. Note that for a sufficient number of cell measurements, the cell size distribution typically converges into a Gaussian (normal) distribution, see Case D in Fig. 20d. However, when the number of measured cells is not sufficiently large, the statistical errors can lead to a cell size distribution that deviates from the Gaussian distribution and might resemble other non-physical distributions, such as a bimodal distribution, see for instance Fig. 20b and c.

Additionally, we validate the suggested computer vision approach by comparing our measured cell sizes against those originally reported by Smirnov et al. [64] for two different numerical soot foils (see Fig. 5a and b in [64]). The computer vision approach cell detection results are shown in Fig. 21a and c. For these soot foils, the reported cell size values, manually measured by Smirnov et al. [64], were 0.2 cm and 0.4 cm for Fig. 21a and c, respectively. The computer vision approach cell size measurements for the cases shown in Fig. 21a and c are 0.218 cm and 0.430 cm, leading to relative errors of 9.0% and 7.5%, respectively. Subsequently, these numerical soot foil images are utilized to qualitatively compare our method contour detection results against the machine-learning-based approach introduced by Sharma et al. [44]. Fig. 21b and d present the cell detection results obtained by the approach suggested by Sharma et al. [44]. A visual inspection of the first numerical soot foil, see Fig. 21a and b, suggests that both automated methods appear to capture most of the cellular structures observed in the image. Nevertheless, for both methods, certain areas containing cellular structures are left undetected. For the second numerical soot foil, see Fig. 21c and d, the machine-learning based approach seems to capture most of the observed cellular structures, whereas our computer vision approach is unable to detect certain areas. The suggested computer vision approach can be further improved by implementing new techniques in the image preprocessing step.

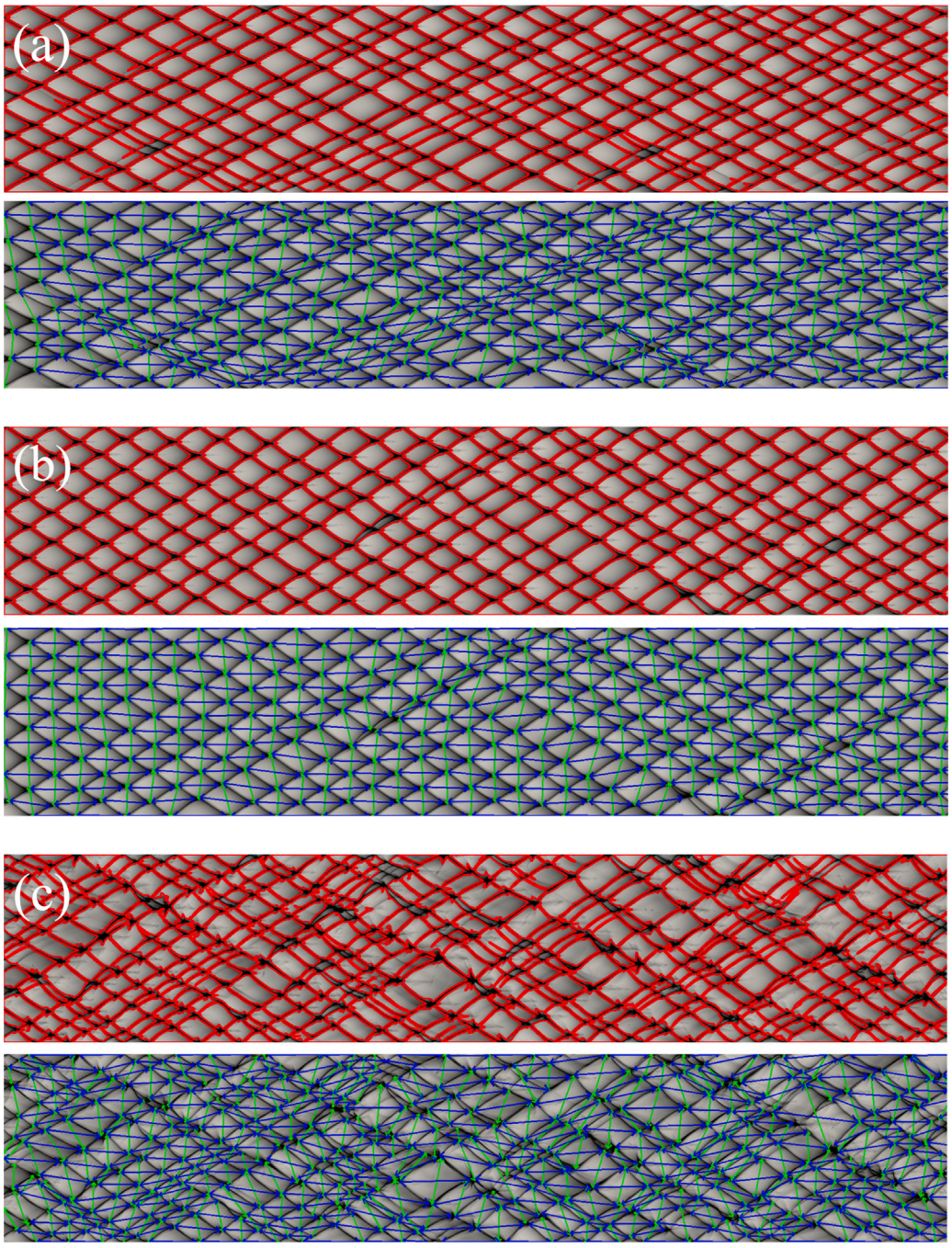

Fig. 15. Numerical soot foils with different levels of cell regularity for $\gamma = 1.4$, $\hat{q} = 25$, and ϵ values of: (a) 2.5, (b) 3.75, and (c) 5. Computer vision approach detection results are overlaid in red, and cell measurements are indicated by green and blue arrows. (For interpretation of the references to color in this figure legend, the reader is referred to the web version of this article.)

We further validate our computer vision approach by analyzing a soot foil image derived via 2-D numerical simulations from the work by Crane et al. [37], see Fig. 22. The automatically measured cell widths and lengths are denoted by violet and green arrows, respectively. Note that the shaded areas in Fig. 22 represent partial cellular structures that are automatically excluded by the computer vision approach from the analysis. Although most of the cell dimensions are detected by the computer vision approach, some individual cells are left undetected. Nevertheless, the following analysis demonstrates that the current results are in accordance with manual measurements. For this purpose, we compare the measured cell width distributions using histograms, see Fig. 23. For both cases, the cell width manual measurements by Crane et al. [37] are compared against our own original cell width manual measurements and the computer vision approach's cell width measurements. There is excellent agreement among the three different cases. In fact, the results indicate that the computer vision approach measurements are very accurate, taking into account the well-known subjective errors induced by manual cell size measurements, see for instance [22].

Finally, we validate our computer vision approach against the manual measurements by Meagher et al. [30]. Seven cases of soot foil images derived via 2-D numerical simulations for gas-phase detonations in different hydrogen–oxygen mixtures are examined, see Figs. 24 and 25. We use the same visualization style for the measured detonation cells as presented in Fig. 22. These seven cases cover a wide range of cellular pattern regularity, from mainly regular to irregular patterns. In

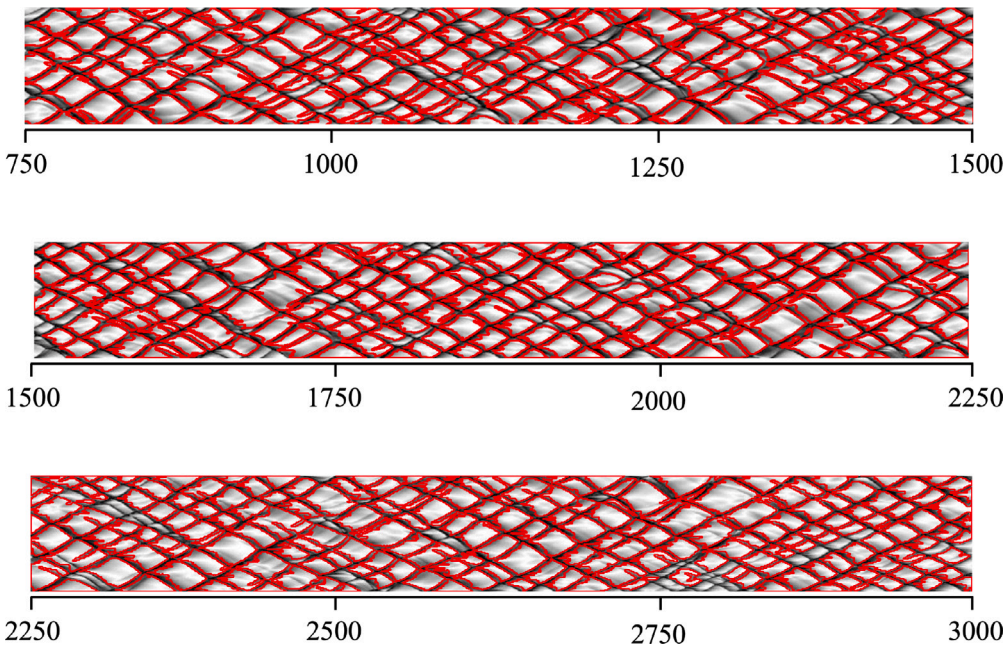

Fig. 16. Detonation cell size measurements for an irregular numerical soot (Case A) from Sharpe and Radulescu [22]. The computer vision approach results are overlaid in red. (For interpretation of the references to color in this figure legend, the reader is referred to the web version of this article.)

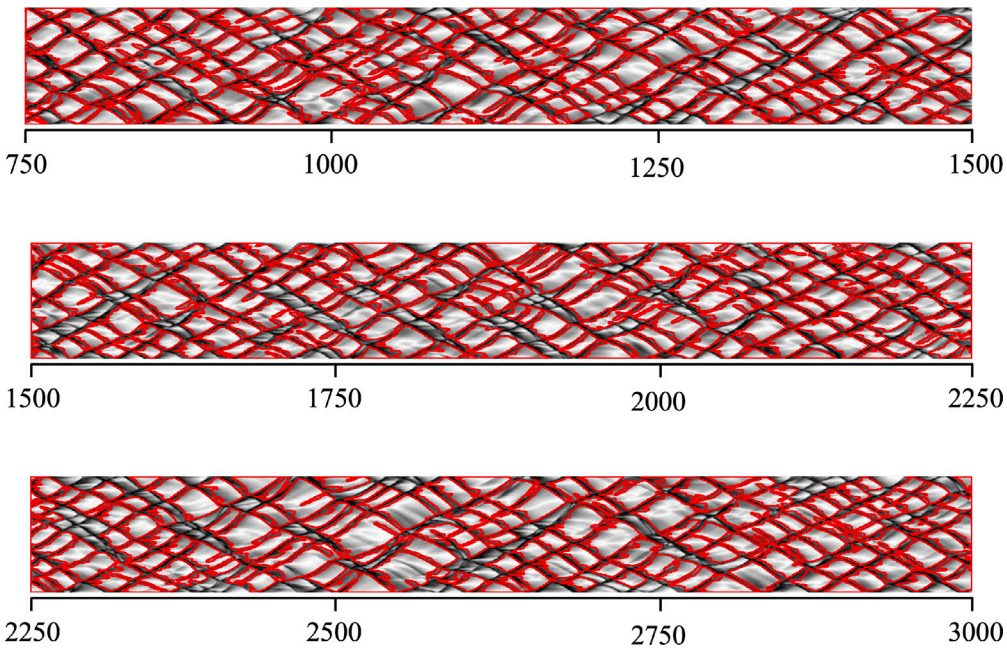

Fig. 17. Detonation cell size measurements for an irregular numerical soot (Case B) from Sharpe and Radulescu [22]. The computer vision approach results are overlaid in red. (For interpretation of the references to color in this figure legend, the reader is referred to the web version of this article.)

addition, the original image quality is much lower than the numerical soot foils analyzed in previous sections. As such, for cases with a very high level of cell irregularity, like 1, 2, 6, and 7, the computer vision approach cannot properly identify the cellular structures in certain areas. We found that the image preprocessing step, see Section 2.1, is the main reason for this discrepancy as it leads to obscure cellular structure in certain areas. Moreover, due to the relatively low image quality, for cases 4, 5, and 6, the computer vision approach sometimes identifies multiple cell widths as a single cell width. Nevertheless, we show below that the computer vision measurements for all the cases are still reasonably aligned with the average cell dimensions as measured manually by Meagher et al. [30]. Thus, for each case, the average cell width, λ, and length, L, normalized by the induction length, Δ_i, are measured by the computer vision approach.

Fig. 26 presents the average normalized cell dimensions according to the manual measurement by Meagher et al. [30] and the measurements by the computer vision approach. Error bars for one standard deviation of the measured values are also shown. One can observe that for all cases the agreement between the two approaches is fairly good, and for almost all of them the average normalized cell length and width values, as obtained from the computer vision approach, fall between the range bounded by the error bars as determined by Meagher et al. [30]. A more quantitative comparison of the measured normalized cell widths and lengths is presented in Table 3. We show measured

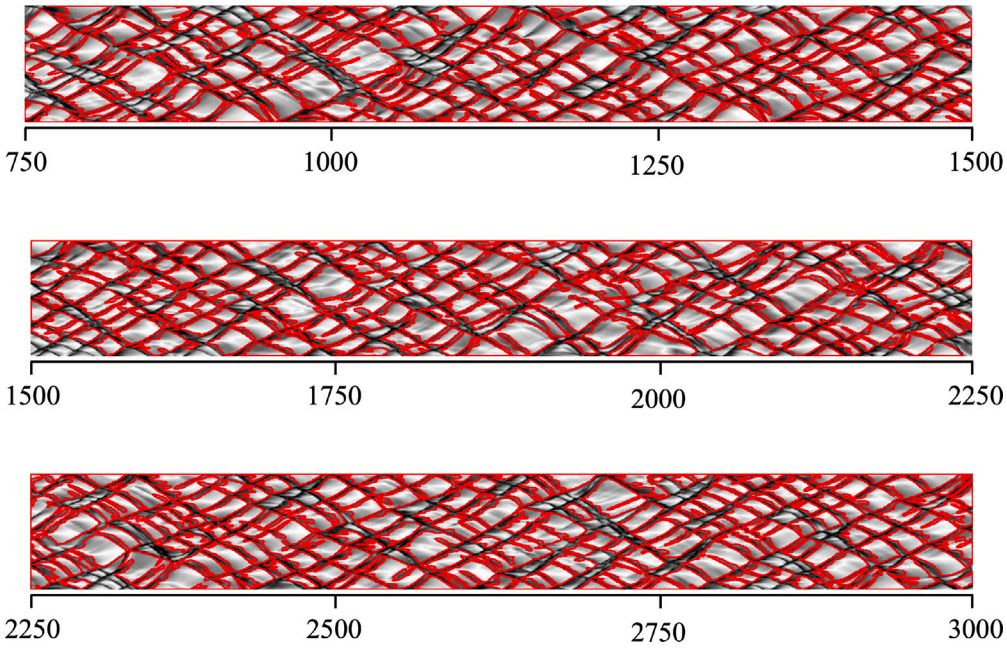

Fig. 18. Detonation cell size measurements for an irregular numerical soot (Case C) from Sharpe and Radulescu [22]. The computer vision approach results are overlaid in red. (For interpretation of the references to color in this figure legend, the reader is referred to the web version of this article.)

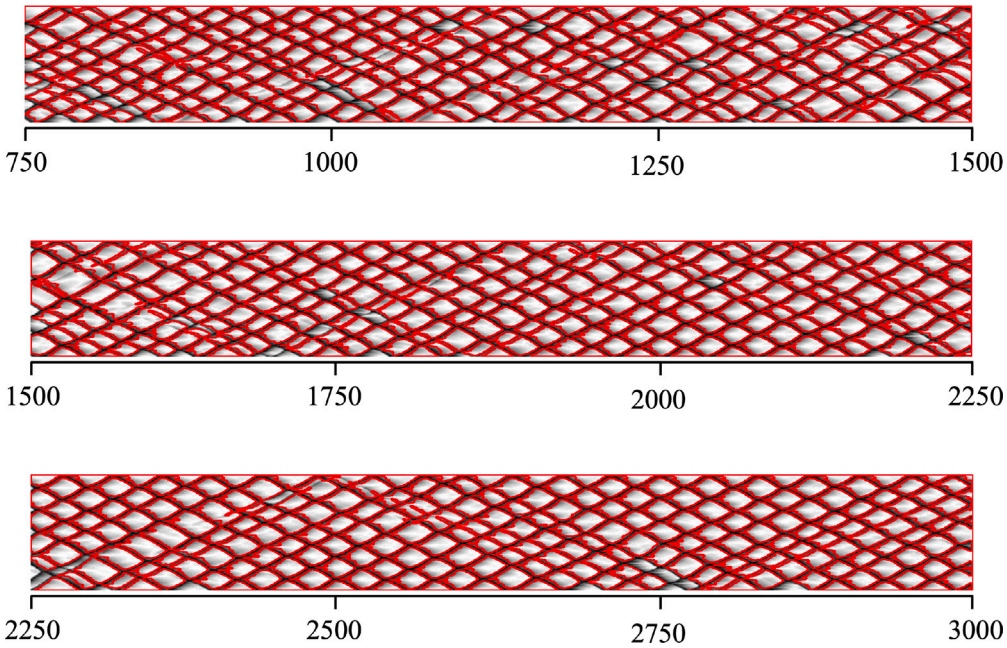

Fig. 19. Detonation cell size measurements for an irregular numerical soot (Case D) from Sharpe and Radulescu [22]. The computer vision approach results are overlaid in red. (For interpretation of the references to color in this figure legend, the reader is referred to the web version of this article.)

values both by Meagher et al. [30] and the computer vision approach including the relative errors. For almost all the seven cases the relative errors are below 20%. The only exceptions are the normalized cell widths in cases 5 and 6 that exhibit relative errors of about 30%. As mentioned above, these differences are associated with the computer vision approach tendency to detect multiple cell widths as a single cell width. These discrepancies could have been avoided by using images with a higher resolution that are currently not available for us. Also, further improvements in the image preprocessing step, see Section 2.1, either by algorithmic or machine-learning-based techniques, can allow better cell detection for low resolution images. These rather challenging test cases demonstrate that even for low resolution soot foil images, in which not all areas are identified or identified incorrectly, the derived average cell dimensions reasonably agree with manual measurement results. This is due to the fact that once a sufficient number of cells are measured by the computer vision approach, the cell size average values can still be accurately captured.

3.5. Analysis of experimentally-obtained cellular structure images

In this section, we demonstrate our computer vision approach's ability to analyze experimentally-obtained detonation cellular structure images. The most common experimental method for measuring the detonation cell dimensions is covering the inner sections of the tube or the

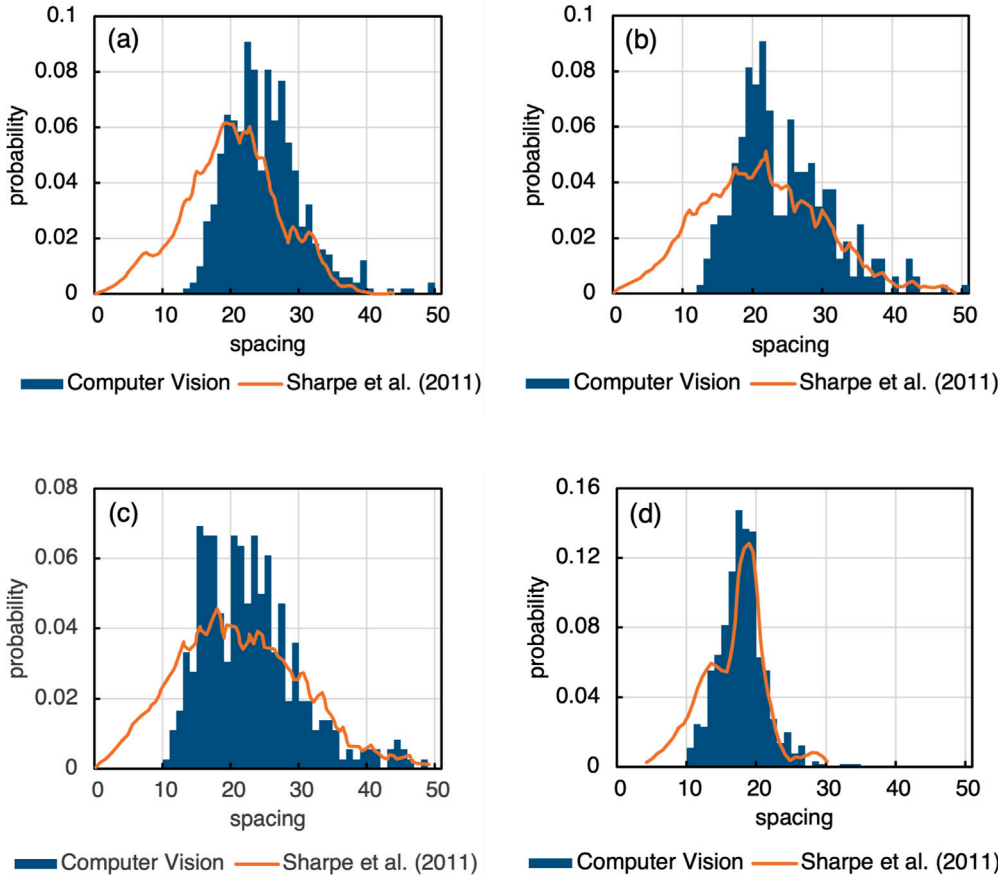

Fig. 20. Statistical analysis for irregular cell size distributions. Comparison between PDFs obtained by Sharpe and Radulescu [22] and histograms obtained by the computer-vision-based approach: (a) Case A ($E = 20$); (b) Case B ($E = 25$); (c) Case C ($E = 27$); (d) Case D ($E = 15$).

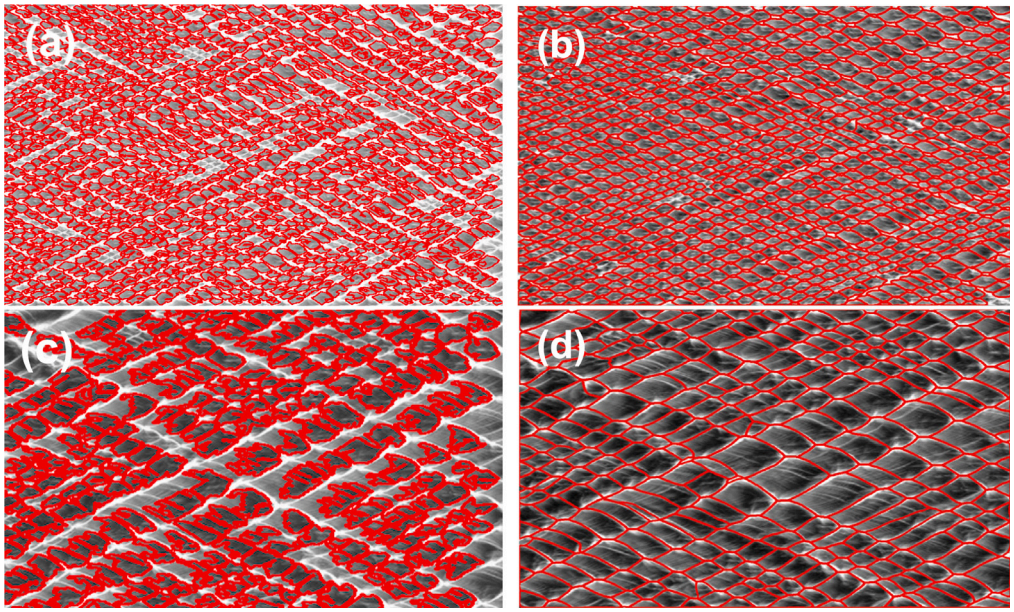

Fig. 21. Comparison of automated cell detection methods applied to numerical soot foils originally presented by Smirnov et al. [64]: Left panel — Results obtained using the proposed computer-vision-based approach. Right panel — Results obtained using the machine-learning-based method proposed by Sharma et al. [44] (reprinted with permission from Elsevier).

channel with soot foils, see for instance [5,8,65] . However, we found that existing experimental soot foil images from the literature contain a significant amount of noise and in many cases the image quality is poor due to external factors, such as smoking technique, camera resolution, and contrast. As a result, the currently suggested image preprocessing step, see Section 2.1, yields black and white images in which a significant portion of the cellular structures is missing. Thus, cell size measurements using the contour detection algorithm, see Section 2.2,

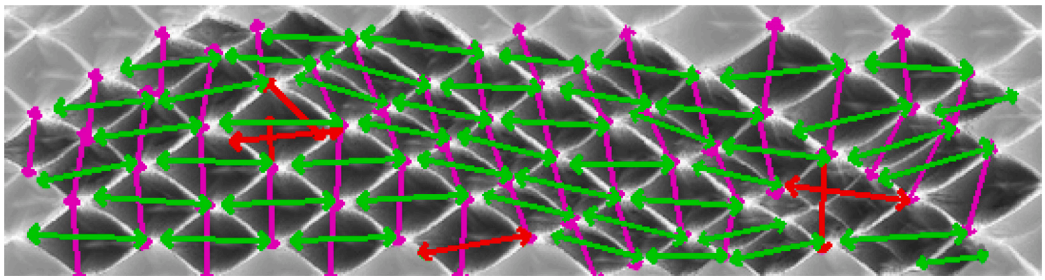

Fig. 22. Computer vision approach cell width and length measurements for the numerical soot foil as obtained from Crane et al. [37]. The shaded areas represent partial cell structures that are automatically excluded from the analysis. The total number of detected cells is 53. Misaligned measurements are indicated by the red arrows (5.66% out of total measured cells). (For interpretation of the references to color in this figure legend, the reader is referred to the web version of this article.)

Table 3
Comparison of average normalized cell dimensions measurements between Meagher et. al [30] and the computer vision approach.

Cell dimension	λ/Δ_i							L/Δ_i						
Case	1	2	3	4	5	6	7	1	2	3	4	5	6	7
Meagher et al. [30]	22.7	20.0	23.1	18.4	18.6	19.5	11.9	33.9	30.0	37.8	31.2	32.6	29.8	17.9
CV approach	25.3	20.6	26.2	20.8	24.3	25.4	13.1	29.0	24.3	33.5	27.3	29.1	30.6	14.7
Total number of measured cells (misaligned measurements)	48 (11)	38 (7)	63 (10)	101 (19)	93 (16)	75 (26)	55 (17)	48 (11)	38 (7)	63 (10)	101 (19)	93 (16)	75 (26)	55 (17)
Relative error, %	11	3.0	14	13	30	30	10	14	19	11	15	11	3.0	18

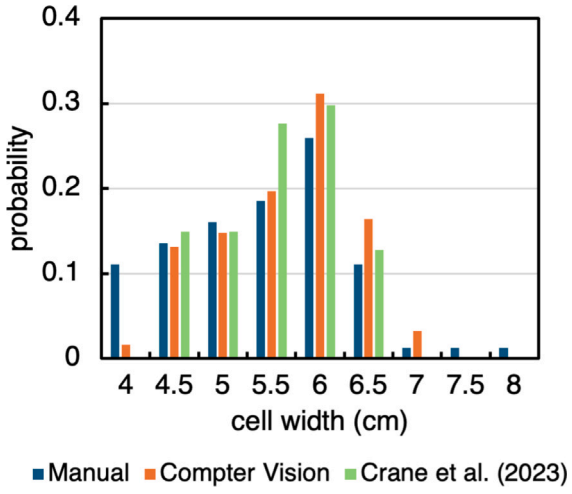

Fig. 23. Statistical analysis for irregular cell size distributions. Comparison by histograms between computer vision approach and manual measurements as obtained by ourselves and by Crane et al. [37].

simply cannot provide accurate measurements for areas with missing cellular structures. It is possible to resolve this limitation by further improving the image preprocessing step either through more advanced algorithmic or machine-learning-based techniques. Nevertheless, we demonstrate that the computer vision approach with the currently suggested image preprocessing step is capable of detecting cellular structures in real experimentally-derived images once the image quality is comparable to numerical soot foils. Another possible technique for experimentally measuring cell dimensions is using open shutter photography, see for instance [10,11]. For this case, the obtained experimental images exhibit similar quality to typical numerical soot foils. Hence, we analyze via the computer vision approach the experimental images obtained by Radulescu and Lee [10] for cellular detonations propagating in thin rectangular channels with partially porous walls. We focus on the case of an acetylene-oxygen (C_2H_2/O_2) stoichiometric mixture with an initial pressure of 3.6 kPa. In the experiments by Radulescu and Lee [10], the detonation wave first propagates under confinement of solid walls and then encounters the porous walled section. As a result of detonation wave interactions with the porous walls, the cell size tends to increase and can even, for some cases, disappear altogether due to detonation attenuation [10]. Figs. 27 and 28 present the open shutter photography images by Radulescu and Lee [10] overlaid with the computer vision approach contour detection and cell size measurements. Three different channels are shown, in which detonation waves propagated simultaneously. Fig. 27 presents the solid wall part of the channel while Fig. 28 presents the porous wall part of the channel. In each image, cell width and length measurements are denoted by violet and green arrows, respectively. The total number of measured cells for the combined solid and porous wall parts is 143, 130, and 144 for the top, middle, and bottom channels, respectively. Misaligned or duplicated measurements were visually and manually assessed, and are marked by red arrows. Moreover, partial detonation cells near the boundaries of the channel are shaded since they are automatically excluded from the analysis. It is evident that most of the cellular structure in the image is identified by the computer vision approach.

We can also use the results to separately analyze the detonation cell size at the solid and the porous wall sections. First, according to the computer vision approach measurements, the average cell widths for the solid and porous wall sections are 8.89 mm and 9.83 mm, respectively. This trend of increasing average cell width due to the presence of porous walls qualitatively agrees with the experimental results. Second, we can compare the average cell width value measured by the computer vision approach at the solid wall section against other measurements from the literature. Nevertheless, it should be noted that existing measured cell width values for these specific conditions exhibit different values. For instance, Strehlow et al. [5] provided cell width measurements for detonation waves propagating in a rectangular channel with an acetylene-oxygen stoichiometric mixture and initial pressure values ranging from 1.5 to 101.3 kPa. The average cell width measured by our computer vision approach for the solid wall section is 8.89 mm, while the interpolated cell size from Strehlow et al. [5] for an initial pressure of 3.6 kPa is 9.13 mm, suggesting a relative error of 2.6%. On the other hand, Radulescu and Lee [10] derived correlations for the cell width as a function of initial pressure for various mixtures. These correlations are based on experiments carried out using a round tube by Desbordes et al. [66,67], Pedley et al. [68], Knystautas et al. [69], Laberge et al. [70], and Abid et al. [71]. For the case of

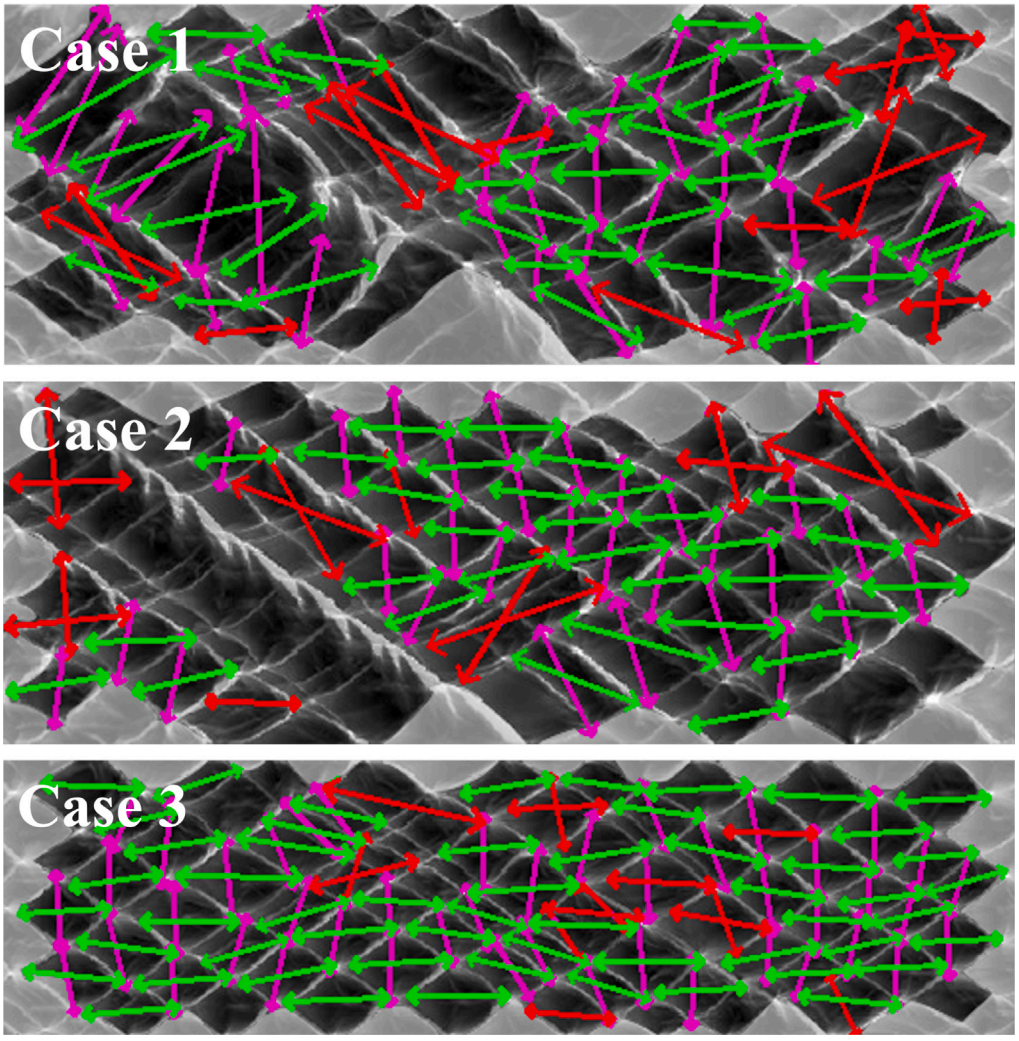

Fig. 24. Computer vision approach cell width and length measurements for the numerical soot foils as obtained from cases 1–3 of Meagher et al. [30]. The shaded areas represent partial cell structures that are automatically excluded from the analysis. Misaligned and duplicated measurements are indicated by the red arrows. (For interpretation of the references to color in this figure legend, the reader is referred to the web version of this article.)

acetylene-oxygen stoichiometric mixtures, the value of the average cell width derived from the correlation is 5.6 mm, while the average cell width value using the computer vision approach is 8.89 mm, suggesting a relative error of 59%.

A more detailed statistical analysis for the cell width and length distributions at solid and porous wall sections is shown in Fig. 29. Both histograms, see Fig. 29a and c, and CDFs, see Fig. 29b and d, are used for comparison between the different cell size distributions. Our analysis shows a notable change in both cell width and length distributions due to the presence of porous walls. Although the values of the minimum cell dimensions are almost unaffected by the porous wall interactions, the cell dimensions distributions for the porous wall section are different from the cell dimensions distributions for the solid wall section. The current analysis demonstrates our computer vision approach's ability to assist in gaining deeper understanding of complex physical phenomena affecting the detonation cellular structure as demonstrated by Radulescu and Lee [10].

4. Conclusions

In the current work, we present a novel computer-vision-based approach for automated detection and statistical analysis of detonation cellular structure images. The proposed method employs advanced image processing techniques, contour detection algorithms, and optimization schemes to accurately identify and measure detonation cell sizes.

We demonstrate that for images with a sufficiently high initial resolution, the proposed computer vision approach can effectively identify and measure the average cell dimensions from numerical soot foils with a wide range of cell regularity levels. In particular, for high-resolution images with regular and irregular cellular patterns, the maximum relative errors for the average cell dimensions are 8% and 17%, respectively. On the other hand, for low-resolution images, the maximum relative errors for the average cell dimensions can increase up to 30%. Moreover, for cases with irregular cellular structures, we carried out a detailed, automatic histogram analysis. The results show that the accuracy of the derived statistics is comparable to manual measurements. Similar trends are observed for comparisons against the automatic signed vorticity record method for mildly irregular cellular patterns. On the other hand, for highly irregular patterns, we found some discrepancies between the two methods in the statistics of very small cellular structures. These discrepancies are attributed to small cells going undetected by the computer vision approach and detection of non-existent small cellular structures by the signed vorticity record method. We also show that the computer vision approach can be used to analyze high-quality experimental images of detonation cellular structures. More specifically, we analyze experimental results under the

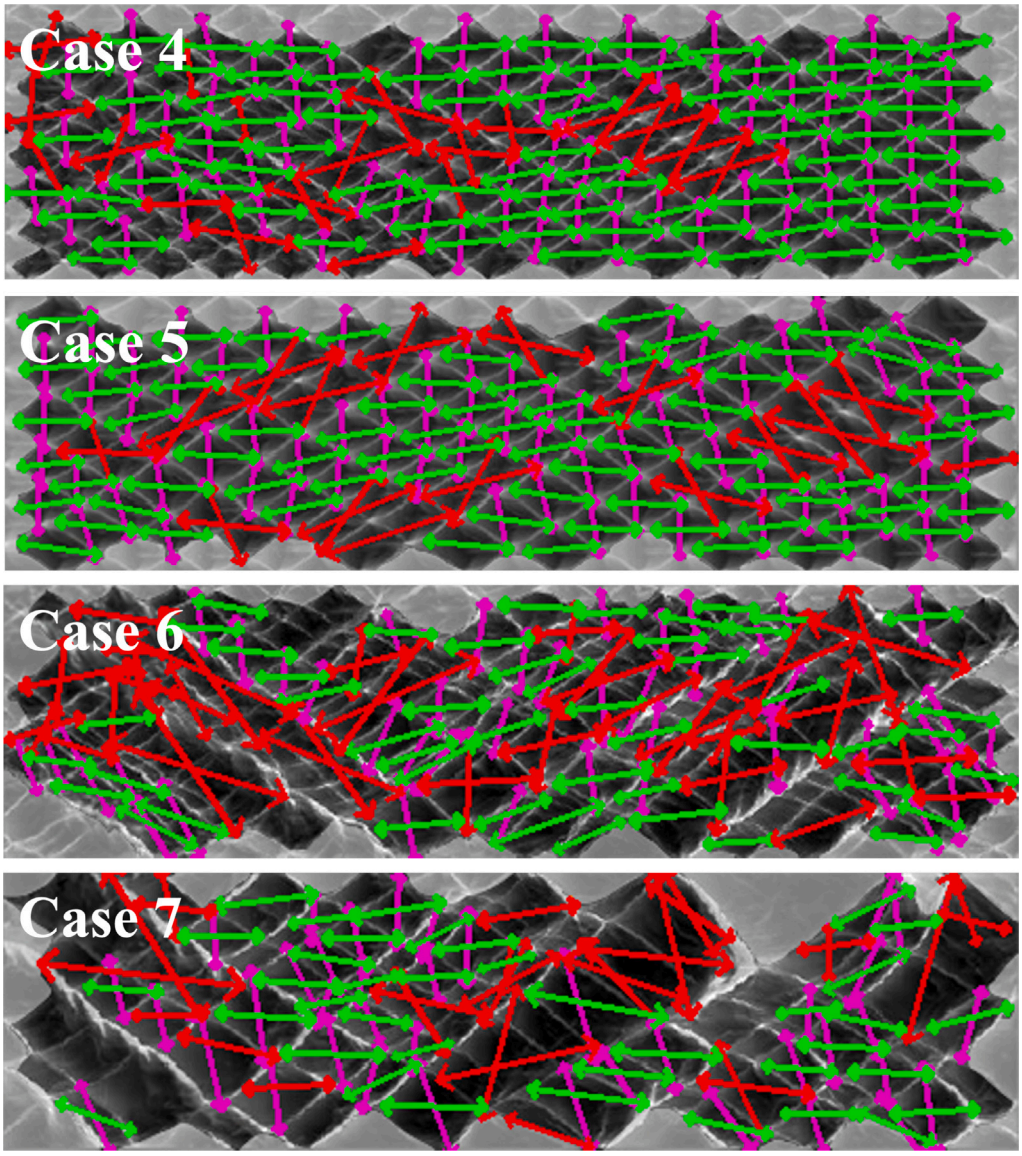

Fig. 25. Computer vision approach cell width and length measurements for the numerical soot foils as obtained from cases 4–7 of Meagher et al. [30]. The shaded areas represent partial cell structures that are automatically excluded from the analysis. Misaligned and duplicated measurements are indicated by the red arrows. (For interpretation of the references to color in this figure legend, the reader is referred to the web version of this article.)

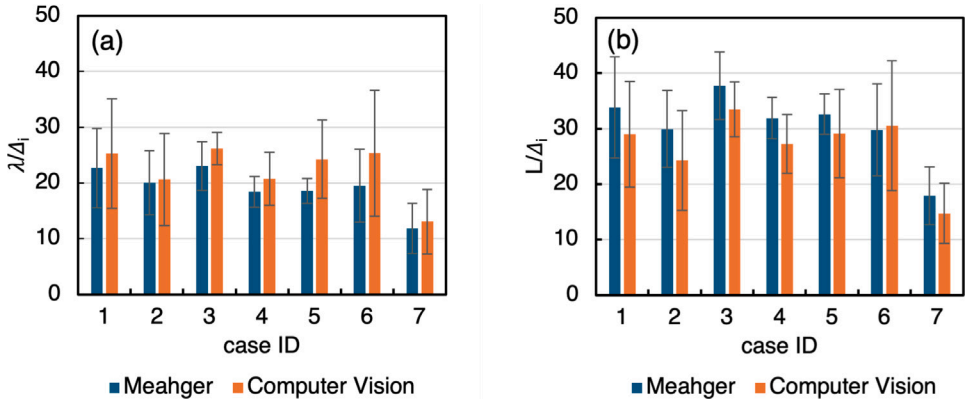

Fig. 26. Statistical analysis for average normalized cell dimensions. Comparison between our computer vision approach measurements and manual measurements by Meagher et al. [30] for: (a) Normalized cell width, λ/Δ_i, and (b) Normalized cell length, L/Δ_i. For each case, error bars at one standard deviation of measured values are presented.

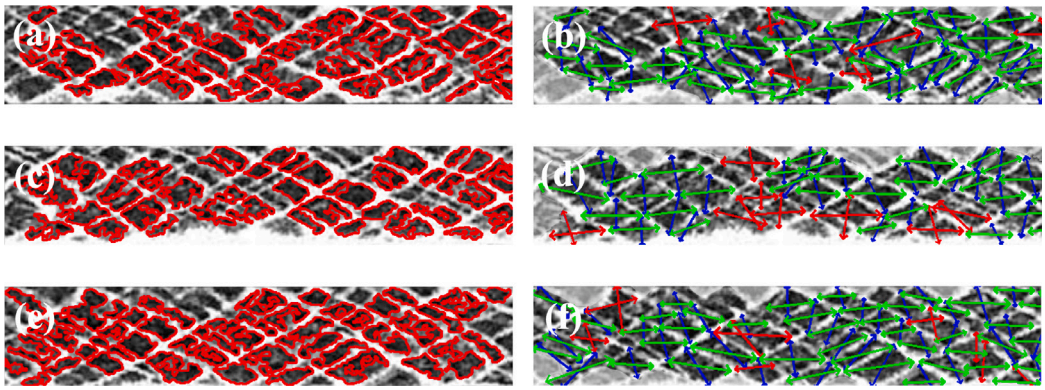

Fig. 27. Computer vision approach contour detection results (left panel) and cell size measurements (right panel) overlaid on the solid wall part in the experimentally-derived detonation cellular structure images by Radulescu and Lee [10]. Clearly visible misaligned or duplicated measurements are marked in red arrows (12.2%, 21.6%, and 17.4% out of the measured cells for (b), (d), and (f), respectively.). (For interpretation of the references to color in this figure legend, the reader is referred to the web version of this article.)

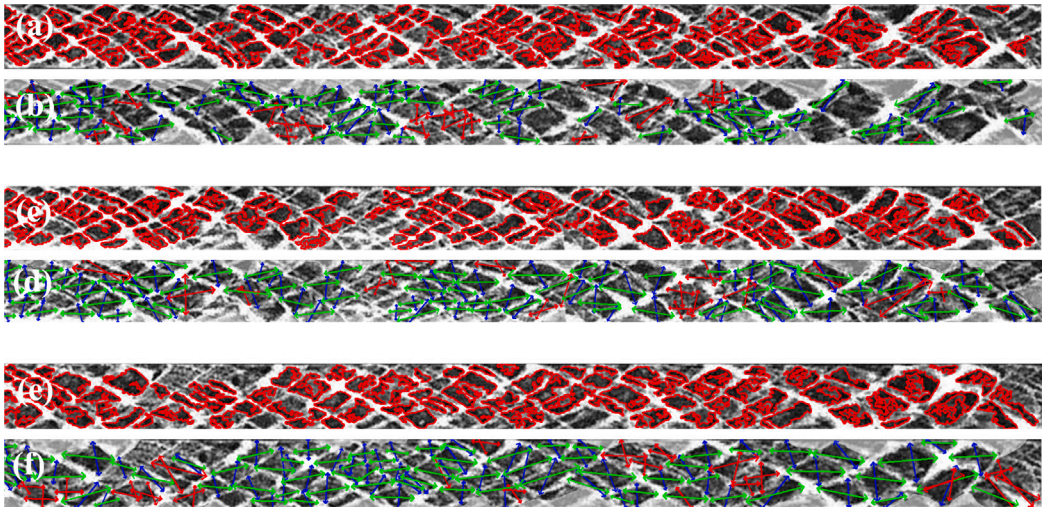

Fig. 28. Computer vision approach contour detection results (see (a), (c), and (e)) and cell size measurements (see (b), (d), and (f)) overlaid on the porous wall part in the experimentally-derived detonation cellular structure images by Radulescu and Lee [10]. Clearly visible misaligned or duplicated measurements are marked in red arrows (29.8%, 18.3%, and 21.4% out of the measured cells for (b), (d), and (f), respectively). (For interpretation of the references to color in this figure legend, the reader is referred to the web version of this article.)

complex scenario of a detonation wave propagating through channels with partially porous walls. We demonstrate our method's ability to quickly measure, compare, and analyze the cell statistics in either solid or porous wall sections. Also, a comparison of the measured average cell width at the solid wall section against experimental measurements from the literature is found to be in reasonable agreement.

The suggested computer vision approach allows quick, accurate, and reliable analysis of detonation cellular structure images, which is independent of subjective measurement errors, as long as the image initial resolution is sufficiently high. As a result, cell size measurement errors, which can explain some of the discrepancies between numerical and experimental results, can be significantly reduced. Finally, we envision that the proposed computer vision approach will serve as a foundation for developing a standardized method for detonation cell size measurements.

CRediT authorship contribution statement

Daniel Jalontzki: Writing – original draft, Visualization, Validation, Methodology, Investigation, Formal analysis, Data curation. **Alon Zussman:** Writing – review & editing, Methodology, Investigation. **Sumedh Pendurkar:** Writing – review & editing, Formal analysis. **Guni Sharon:** Writing – review & editing, Supervision, Project administration, Funding acquisition. **Yoram Kozak:** Writing – review & editing, Supervision, Project administration, Funding acquisition, Conceptualization.

Declaration of competing interest

The authors declare that they have no known competing financial interests or personal relationships that could have appeared to influence the work reported in this paper.

Acknowledgments

We would like to thank the U.S.-Israel Binational Science Foundation (BSF) for funding the research project "Modeling and Analysis of Heavy Hydrocarbon Liquid Fuel Spray Detonations", Application Number: 2022191. D.J. would also like to thank the Israeli Ministry of Energy for partially funding his fellowship.

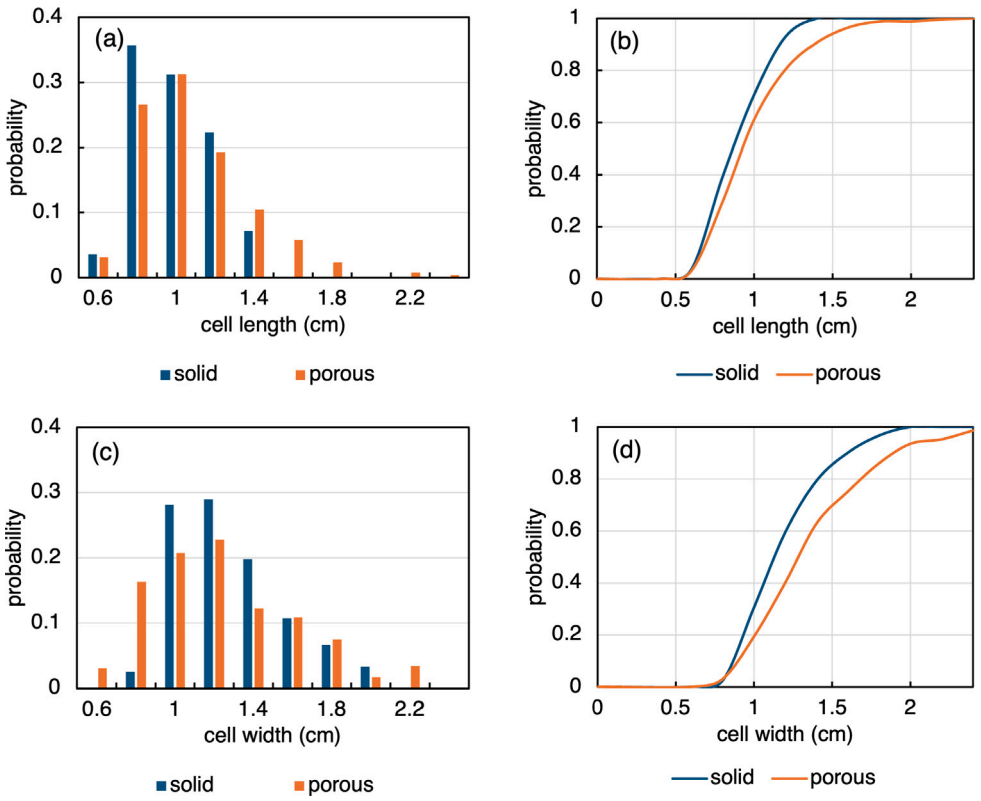

Fig. 29. Statistical analysis of experimental images from Radulescu and Lee [10] for cell dimensions based on the computer vision approach. Comparison between solid and porous wall sections: (a) Cell length histogram, (b) Cell length CDF, (c) Cell width histogram, (d) Cell width CDF.

Data availability

The data will be shared via an online repository.

References

[1] Gross RA, Oppenheim A. Recent advances in gaseous detonation. ARS J 1959;29:173–9.
[2] Papavassiliou J, Makris A, Knystautas R, Lee J, Westbrook C, Pitz W. Measurements of cellular structure in spray detonation. Progr Astronaut Aeronaut 1993;154. 148–169.
[3] Lee JH. The detonation phenomenon. Cambridge University Press; 2008.
[4] Fickett W, Davis WC. Detonation: theory and experiment. Courier Corporation; 2000.
[5] Strehlow RA, Maurer RE, Rajan S. Transverse waves in detonations. I-Spacing in the hydrogen-oxygensystem. AIAA J 1969;7:323–8.
[6] Lee JH. Dynamic parameters of gaseous detonations. Annu Rev Fluid Mech 1984;16:311–36.
[7] Desbordes D, Presles H-N. Multi-scaled cellular detonation. In: Shock waves science and technology library. Vol. 6, Springer; 2012, p. 281–338.
[8] Shepherd JE. Detonation in gases. Proc Combust Inst 2009;32:83–98.
[9] Oran ES, Chamberlain G, Pekalski A. Mechanisms and occurrence of detonations in vapor cloud explosions. Prog Energy Combust Sci 2020;77:100804.
[10] Radulescu MI, Lee JH. The failure mechanism of gaseous detonations: experiments in porous wall tubes. Combust Flame 2002;131:29–46.
[11] Radulescu MI, Maxwell BM. The mechanism of detonation attenuation by a porous medium and its subsequent re-initiation. J Fluid Mech 2011;667:96–134.
[12] Tieszen SR, Stamps DW, Westbrook CK, Pitz WJ. Gaseous hydrocarbon - air detonations. Combust Flame 1991;84:376–90.
[13] Ciccarelli G, Ginsberg T, Boccio J, Economos C, Sato K, Kinoshita M. Detonation cell size measurements and predictions in hydrogen-air-steam mixtures at elevated temperatures. Combust Flame 1994;99:212–20.
[14] Ciccarelli G, Card J. Detonation in mixtures of JP-10 vapor and air. AIAA J 2006;44:362–7.
[15] Ng HD, Chao J, Yatsufusa T, Lee JH. Measurement and chemical kinetic prediction of detonation sensitivity and cellular structure characteristics in dimethyl ether–oxygen mixtures. Fuel 2009;88:124–31.
[16] Mével R, Davidenko D, Lafosse F, Chaumeix N, Dupré G, Paillard C-É, Shepherd JE. Detonation in hydrogen–nitrous oxide–diluent mixtures: An experimental and numerical study. Combust Flame 2015;162:1638–49.
[17] Schumaker SA, Knisely AM, Hoke JL, Rein KD. Methane–oxygen detonation characteristics at elevated pre-detonation pressures. Proc Combust Inst 2021;38:3623–32.
[18] Shi X, Jayaraman AS, Wang H. Probing vibrational nonequilibrium in detonations with ozone. Proc Combust Inst 2024;40:105695.
[19] Kadosh H, Michaels D. Measurement of detonation cell size in liquid ethanol and oxygen mixtures. Shock Waves 2022;32:231–4.
[20] Brown T, Hytovick R, Berson J, Burke R, Salauddin S, Ahmed K. Dynamics of mono-size aerosolized liquid fuel detonations. Proc Combust Inst 2024;40:105416.
[21] Zadok N, Oruganti SK, Alves MM, Kozak Y. Dimensional analysis and simplified modeling for the cellular structure of premixed gas-phase detonation numerical simulations with single-step kinetics. Combust Flame 2023;256:112954.
[22] Sharpe G, Radulescu M. Statistical analysis of cellular detonation dynamics from numerical simulations: One-step chemistry. Combust Theor Model 2011;15:691–723.
[23] Lu X, Kaplan CR, Oran ES. A chemical-diffusive model for simulating detonative combustion with constrained detonation cell sizes. Combust Flame 2021;230:111417.
[24] Gamezo VN, Desbordes D, Oran ES. Formation and evolution of two-dimensional cellular detonations. Combust Flame 1999;116:154–65.
[25] Gamezo V, Desbordes D, Oran E. Two-dimensional reactive flow dynamics in cellular detonation waves. Shock Waves 1999;9:11–7.
[26] Gavrikov A, Efimenko A, Dorofeev S. A model for detonation cell size prediction from chemical kinetics. Combust Flame 2000;120:19–33.
[27] Sow A, Lau-Chapdelaine S-M, Radulescu M. The effect of the polytropic index γ on the structure of gaseous detonations. Proc Combust Inst 2021;38:3633–40.
[28] Taileb S, Melguizo-Gavilanes J, Chinnayya A. The influence of the equation of state on the cellular structure of gaseous detonations. Phys Fluids 2021;33.
[29] Weng Z, Mével R. Dynamics of detonation cellular structure in linear and nonlinear instability regimes. Proc Combust Inst 2024;40:105438.
[30] Meagher PA, Shi X, Santos JP, Muraleedharan NK, Crane J, Poludnenko AY, Wang H, Zhao X. Isolating gasdynamic and chemical effects on the detonation cellular structure: A combined experimental and computational study. Proc Combust Inst 2023;39:2865–73.
[31] Taylor B, Kessler D, Gamezo V, Oran E. Numerical simulations of hydrogen detonations with detailed chemical kinetics. Proc Combust Inst 2013;34:2009–16.

[32] Araki T, Yoshida K, Morii Y, Tsuboi N, Hayashi AK. Numerical analyses on ethylene/oxygen detonation with multistep chemical reaction mechanisms: grid resolution and chemical reaction model. Combust Sci Technol 2016;188:346–69.
[33] Veiga-López F, Taileb S, Chinnayya A, Melguizo-Gavilanes J. Towards predictive simplified chemical kinetics for hydrogen detonations. Combust Flame 2024;269:113710.
[34] Sankar V, Chatelain KP, Lacoste DA. Evaluation of chemical kinetic models for simulations of hydrogen detonations by comparison with experimental data. Appl Energy Combust Sci 2024;100306.
[35] Williams DN, Bauwens L, Oran ES. Detailed structure and propagation of three-dimensional detonations. Symp (Int) Combust 1996;26:2991–8.
[36] Hanana M, Lefebvre M, Van Tiggelen P. On rectangular and diagonal three-dimensional structures of detonation waves. In: Gaseous and heterogeneous detonations: science to applications. ENAS Moscow; 1999, p. 121–30.
[37] Crane J, Lipkowicz JT, Shi X, Wlokas I, Kempf AM, Wang H. Three-dimensional detonation structure and its response to confinement. Proc Combust Inst 2023;39:2915–23.
[38] Tsuboi N, Katoh S, Hayashi AK. Three-dimensional numerical simulation for hydrogen/air detonation: Rectangular and diagonal structures. Proc Combust Inst 2002;29:2783–8.
[39] Moen I, Murray S, Bjerketvedt D, Rinnan A, Knystautas R, Lee J. Diffraction of detonation from tubes into a large fuel-air explosive cloud. Symp (Int) Combust 1982;19:635–44.
[40] Shepherd J, Tieszen S. Detonation cellular structure and image processing. Tech. rep., Sandia National Labs., Albuquerque, NM (USA); 1986.
[41] Shepherd J, Moen I, Murray S, Thibault P. Analyses of the cellular structure of detonations. Symp (Int) Combust 1988;21:1649–58.
[42] Lee J, Frost D, Lee J, Knystautas R. Digital signal processing analysis of soot foils. Prog Astronaut Aeronaut 1993;153. 182–182.
[43] Lee J, Garinis D, Frost D, Lee J, Knystautas R. Two-dimensional autocorrelation function analysis of smoked foil patterns. Shock Waves 1995;5:169–74.
[44] Sharma V, Ullman M, Raman V. A machine learning based approach for statistical analysis of detonation cells from soot foils. Combust Flame 2025;274:114026.
[45] Stockman G, Shapiro LG. Computer vision. Prentice Hall PTR; 2001.
[46] Heymann F, Quest H, Garcia TL, Ballif C, Galus M. Reviewing 40 years of artificial intelligence applied to power systems–a taxonomic perspective. Energy AI 2024;15:100322.
[47] Heikkonen J. A computer vision approach to air flow analysis. Pattern Recognit 1996;17:369–85.
[48] Iglesias G, Ibáñez O, Castro A, Rabuñal J, Dorado J. Computer vision applied to wave flume measurements. Ocean Eng 2009;36:1073–9.
[49] Kulju S, Riegger L, Koltay P, Mattila K, Hyväluoma J. Fluid flow simulations meet high-speed video: computer vision comparison of droplet dynamics. J Colloid Interface Sci 2018;522:48–56.
[50] Kozlowski PM, Kim Y, Haines BM, Robey H, Murphy TJ, Johns HM, Perry TS. Use of computer vision for analysis of image datasets from high temperature plasma experiments. Rev Sci Instrum 2021;92.
[51] Gluzman I, Thomas FO. Characterization of bubble dynamics in the nozzle flow of aviation fuels via computer vision tools. Int J Multiph Flow 2022;154:104133.
[52] Vianna FD, Farenzena B, Pinho MS, Silvestrini JH. Spatiotemporal flow features in gravity currents using computer vision methods. Comput Geosci 2022;165:105146.
[53] Hebral J, Shepherd J. User guide for detonation cell size measurement using photoshop and matlab. In: Explosion dynamics Lab., California Inst. of Technology Rept. FM00-6, Pasadena, CA. 2000.
[54] Bradski G. The OpenCV library. Dr Dobb's J Softw Tools 2000.
[55] Pizer SM, Amburn EP, Austin JD, Cromartie R, Geselowitz A, Greer T, ter Haar Romeny B, Zimmerman JB, Zuiderveld K. Adaptive histogram equalization and its variations. Comput Graph Image Process 1987;39:355–68.
[56] Musa P, Rafi FA, Lamsani M. A review: Contrast-limited adaptive histogram equalization (CLAHE) methods to help the application of face recognition. In: 2018 third international conference on informatics and computing. ICIC, IEEE; 2018, p. 1–6.
[57] Rafael C, Woods REG. Digital image processing. 3rd ed.. Prentice Hall; 2008, p. 687–8.
[58] Otsu N. A threshold selection method from gray-level histograms. IEEE Trans Syst Man Cybern Syst 1979;9:62–6.
[59] Buades A, Coll B, Morel J-M. Non-local means denoising. Image Process Line 2011;1:208–12.
[60] Suzuki S, Abe K. Topological structural analysis of digitized binary images by border following. Comput Graph Image Process 1985;30:32–46.
[61] Monnier V, Vidal P, Rodriguez V, Zitoun R. From graph theory and geometric probabilities to a representative width for three-dimensional detonation cells. Combust Flame 2023;256:112996.
[62] Collins TJ. Imagej for microscopy. Biotechniques 2007;43:S25–30.
[63] Taylor B, Kessler D, Gamezo V, Oran ES. The influence of chemical kinetics on the structure of hydrogen-air detonations. In: 50th AIAA aerospace sciences meeting including the new horizons forum and aerospace exposition. 2012, p. 979.
[64] Smirnov N, Nikitin V, Mikhalchenko E, Stamov L, Tyurenkova V. Modelling cellular structure of detonation waves in hydrogen-air mixtures. Int J Hydrog Energy 2023;49:495–509.
[65] Strehlow RA, Crooker AJ. The structure of marginal detonation waves. Acta Astronaut 1974;1:303–15.
[66] Desbordes D. Transmission of overdriven plane detonations: Critical diameter as a function of cell regularity and size. Prog Astronaut Aeronaut 1988;114:170–85.
[67] Desbordes D, Guerraud C, Hamada L, Presles HN. Failure of the classical dynamic parameters relationships in highly regular cellular detonation systems. Prog Astronaut Aeronaut 1993;153:347–59.
[68] Pedley MD, Bishop CV, Benz FJ, Bennett CA, McClenagan RD, Fenton D, Knystautas R, Lee JH, Peraldi O, Dupre G, Shepherd J. Hydrazine vapor detonations. Prog Astronaut Aeronaut 1988;114:45–63.
[69] Knystautas R, Lee J, Guirao C. The critical tube diameter for detonation failure in hydrocarbon-air mixtures. Combust Flame 1982;48:63–83.
[70] Laberge S, Knystautas R, Lee JHS. Propagation and extinction of detonation waves in tube bundles. Prog Astronaut Aeronaut 1993;153:381–96.
[71] Abid S, Dupre G, Paillard C. Oxidation of gaseous unsymmetrical dimethylhydrazine at high temperatures and detonation of UDMH/O2 mixtures. Prog Astronaut Aeronaut 1991;153:162–81.